POLITECNICO DI TORINO
Repository ISTITUZIONALE

Kinematic modeling, design, and testing of MoviWE.Q, a pseudo-omnidirectional electric-powered wheelchair for indoor mobility

Original
Kinematic modeling, design, and testing of MoviWE.Q, a pseudo-omnidirectional electric-powered wheelchair for indoor mobility / Tagliavini, L., Botta, A., Colucci, G., Baglieri, L., Duretto, S., Toccaceli, L., Amodio, F., Quaglia, G.. - In: MECHANISM AND MACHINE THEORY. - ISSN 0094-114X. - 232:(2026), pp. 1-31. [10.1016/j.mechmachtheory.2026.106690]

Availability:
This version is available at: 11583/3018388 since: 2026-11-25T08:00:33Z

Publisher:
Elsevier

Published
DOI:10.1016/j.mechmachtheory.2026.106690

Terms of use:

This article is made available under terms and conditions as specified in the corresponding bibliographic description in the repository

Publisher copyright

(Article begins on next page)

28 November 2026

Mechanism and Machine Theory 232 (2026) 106690

Contents lists available at ScienceDirect

Mechanism and Machine Theory

journal homepage: www.elsevier.com/locate/mechmt

Research paper

Kinematic modeling, design, and testing of MoviWE.Q, a pseudo-omnidirectional electric-powered wheelchair for indoor mobility

Luigi Tagliavini *, Andrea Botta, Giovanni Colucci, Lorenzo Baglieri, Simone Duretto, Lorenzo Toccaceli, Francesco Amodio, Giuseppe Quaglia

Department of Mechanical and Aerospace Engineering (DIMEAS) - Politecnico di Torino, Corso Duca degli Abruzzi, 24, Torino, 10129, Piemonte, Italy

ARTICLE INFO

Keywords:
Electric powered wheelchair
Omnidirectional mobility
Swerve-drive locomotion
Force-sensitive drive interface
Experimental testing

ABSTRACT

This paper presents the kinematic modeling, design, and experimental validation of MoviWE.Q, an innovative pseudo-omnidirectional electric-powered wheelchair (EPW) developed for indoor mobility. Conventional differential-drive EPWs struggle with maneuverability in confined spaces, while special-wheeled omnidirectional designs suffer from vibrations, noise, and low load capacity. To address these limitations, MoviWE.Q utilizes two swerve-drive locomotion units with standard conventional wheels. The platform integrates manual driving and caregiver-assisted driving via SensHB.Q, a cost-effective force-sensitive interface featuring three uniaxial load cells and compliant flexure joints. A complete kinematic model is formulated to manage actuation redundancy and determine system velocity twist limits. ISO 7176 – 5 tests and indoor navigation trials suggest excellent maneuverability in tight, cluttered environments. Furthermore, caregiver drive evaluations resulted in high usability scores, achieving a System Usability Scale (SUS) score of 83.1 and a low perceived workload (NASA-TLX score of 10.9).

1. Introduction

1.1. Research context

Population aging has become a major global issue, driven by low birth rates and increasing life expectancy [1]. Globally, life expectancy at birth reached 73.3 years in 2024, an increase of 8.4 years since 1995 [2]. On one side, this increase in life expectancy is a positive fact, resulting from better health care and hygiene, healthier lifestyles, better nutrition, and reduced child mortality.

* Corresponding author.
E-mail addresses: luigi.tagliavini@polito.it (L. Tagliavini), andrea.botta@polito.it (A. Botta), giovanni_colucci@polito.it (G. Colucci), lorenzo.baglieri@polito.it (L. Baglieri), simone.duretto@polito.it (S. Duretto), lorenzo.toccaceli@polito.it (L. Toccaceli), francesco.amodio@polito.it (F. Amodio), giuseppe.quaglia@polito.it (G. Quaglia).
URL: https://www.polito.it/en/staff?p=luigi.tagliavini (L. Tagliavini), https://www.polito.it/en/staff?p=andrea.botta (A. Botta), https://www.polito.it/en/staff?p=giovanni_colucci (G. Colucci), https://www.polito.it/didattica/dottorato-di-ricerca/alumni?p=065110 (L. Baglieri), https://www.polito.it/en/staff?p=simone.duretto (S. Duretto), https://www.polito.it/en/staff?p=lorenzo.toccaceli (L. Toccaceli), https://www.polito.it/en/staff?p=francesco.amodio (F. Amodio), https://www.polito.it/en/staff?p=giuseppe.quaglia (G. Quaglia)

https://doi.org/10.1016/j.mechmachtheory.2026.106690
Received 18 September 2026; Received in revised form 29 October 2026; Accepted 11 November 2026
Available online 24 November 2026
0094-114X/© 2026 The Author(s). Published by Elsevier Ltd. This is an open access article under the CC BY-NC-ND license (http://creativecommons.org/licenses/by-nc-nd/4.0/).

Nevertheless, this society improvement is not balanced by an increase in quality of life for the elderly. As reported by Brown in [3] while investigating the current focus of medical research on increasing the quantity, rather than the quality, of life *"…years are being added to our lives, life is not being added to our years: the extra years are being added at the very end of our lives and are of poor quality"*. Population aging impacts various socioeconomic sectors, including family structures, healthcare, housing, and transportation [1]. As reported by the World Health Organization (WHO) in [2] *"This demographic shift has significant implications for public health. Maintaining good health is crucial for older people to remain independent and actively participate in family and community life."* The percentage of the global population 60 years or older rose from 9.2% in 1990 to 11.7% in 2013; between 2015 and 2050, the proportion of the world's population over 60 years will nearly double from 12% to 22% [2,4]. Italy is characterized as having one of the most pronounced aging processes in the world and specifically within the European Union. As of January 1, 2026, there are 14.8 million citizens aged 65 and over, representing 25.1% of the total population [5].

Within this context, assistive technologies play a fundamental role in the lives of many people. Globally, more than 2.5 billion people need one or more assistive products, and an estimated 3.5 billion people will need assistive technology by 2050, as reported by the WHO [6]. Assistive technologies range from physical products such as wheelchairs, glasses, prosthetic limbs, white canes, and hearing aids to digital solutions such as speech recognition or time management software and captioning. They are particularly adopted by older people, people with disabilities, and people with long term health conditions. The WHO Global report on health equity [7] states that the people with disabilities worldwide are more than 1.3 billion, 16% of the global population. There is limited data on the number of people who need wheelchairs; however, the WHO has estimated that at least 80 million people (or 1% of the world's population) are likely to require a wheelchair for daily mobility [6]. The adoption of appropriate wheelchairs facilitates mobility, improving individuals' access to education and employment while reducing healthcare costs due to a reduction in secondary complications such as pressure sores and contractures [6]. In Italy, the Italian National Institute of Statistics (ISTAT) data indicates that approximately 2.833 million people over 65 have significant difficulty walking or climbing stairs without assistance [8]. The WHO and UNICEF Global report on assistive technology [9] shows that the most frequently reported barrier to assistive products access across surveyed countries is affordability, followed by lack of support and lack of availability. Also, the majority of people interviewed in the survey reported that they acquire their assistive products from the private sector, paid for either by themselves, or with financial support from family and friends. On top of the economic barrier, people using wheelchairs or other mobility devices face physical barriers in private and public places. Globally, only about 70% of transit stations are wheelchair-accessible, and about 20% of hospitals and 32% of pharmacies are not accessible for wheelchair users [10]. In Italy, accessibility gaps are also evident in education, with only 41% of schools that are accessible to children with motor disabilities[11].

1.2. Electric-powered wheelchair state-of-the-art

Wheelchairs are generally classified into two primary categories: manual and motorized, the latter of which are also referred to as electric-powered wheelchairs (EPWs). In manual wheelchairs, the system is propelled by the user's muscular force, whereas in EPWs, traction is generated by electric motors.

Manual wheelchairs are mainly utilized for daily mobility and sports. Their widespread adoption is attributed to several key advantages, including cost-effectiveness, reduced maintenance requirements, ease of transport, and the physiological and psychological benefits of physical activity, which can positively influence both cardiovascular health and mood. Despite these benefits, manual devices demand significant upper-body strength and balance. A critical drawback of traditional manual propulsion is the high risk of repetitive strain. Indeed, shoulder pathologies affect over 70% of manual wheelchair users [12].The prevalence of injury is largely linked to the fixed trajectories of conventional propulsion systems. In handrim and lever-based systems, the propulsion motion is constrained to an arc centered on the main wheel axis or the lever's revolute joint, respectively. In hand-bikes, the trajectory is a fixed circumference centered on the crankshaft. These rigid kinematic constraints force the user's musculoskeletal system to adapt to the machine rather than the inverse, often leading to joint degradation. To mitigate these issues, researchers have explored alternative propulsion mechanisms. A notable example is the Handwheelchair.q, a manual wheelchair designed for daily use that employs a rowing-inspired motion and a cable drive mechanism to optimize biomechanical efficiency [13,14].

Electric-powered wheelchairs (EPWs) significantly reduce the physical effort required for mobility, offering various control interfaces tailored to individual user preferences and needs. Furthermore, customized accessories can be integrated to enhance ergonomic comfort. However, these benefits are frequently offset by increased mass and larger dimensions compared to manual wheelchairs, which can complicate transport and limit maneuverability within confined spaces. EPWs are generally classified according to their intended application environment, drive system, and control interface.

The operational environment, indoor or outdoor, dictates specific performance requirements, including speed range, maneuverability, stability, and the ability to deal with the presence of obstacles or uneven terrain. Indoor wheelchairs prioritize high maneuverability and typically operate within a limited speed range. In contrast, outdoor models are designed for higher speeds and must possess the ability to traverse ground irregularities or overcome small steps. Architectural barriers remain a primary challenge for outdoor mobility, prompting the research community to develop specialized obstacle-climbing mechanisms, though few have achieved commercial success (e.g., Scewo BRO). A comprehensive review of the mechanisms and operational sequences for step-climbing wheelchairs was published in 2017 [15]. Based on this analysis, these advanced systems are categorized into four distinct architectural types: leg-wheel hybrid wheelchairs [16–18], tripod-based systems [19,20], rigid support designs [21,22], and tracked systems [23,24].

Most commercially available EPWs utilize differential-drive locomotion, a system consisting of two independent traction wheels mounted on a common axis. This configuration inherently restricts movement to a $2D$ plane. To maintain balance, stability is typically

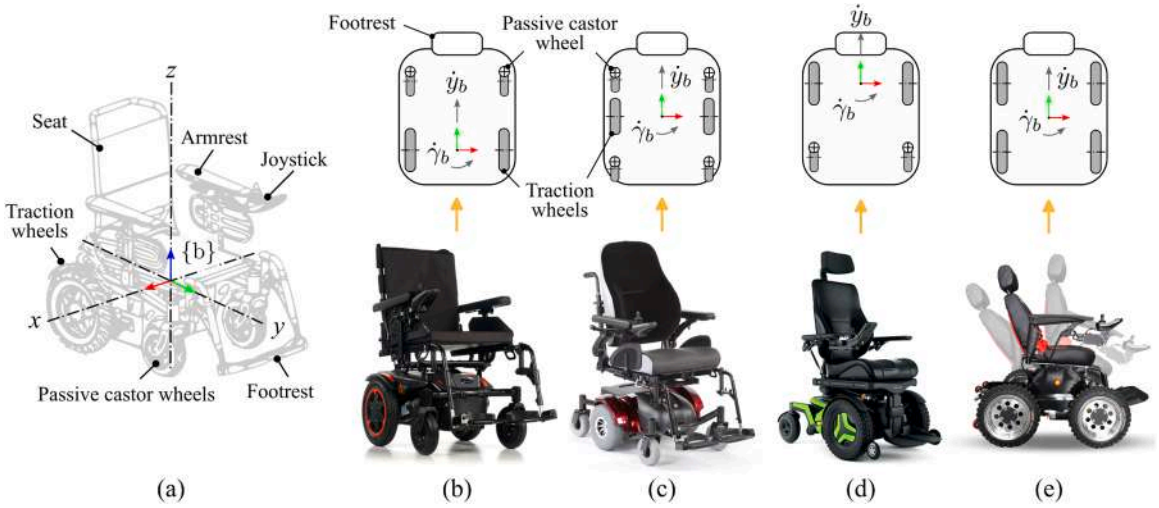

Fig. 1. Examples of differential-drive EPWs: (a) schematic representation of a rear drive EPW and reference frame definition, (b) rear drive [25], (c) middle drive [26], (d) front drive [27], (e) four driven-wheels [28].

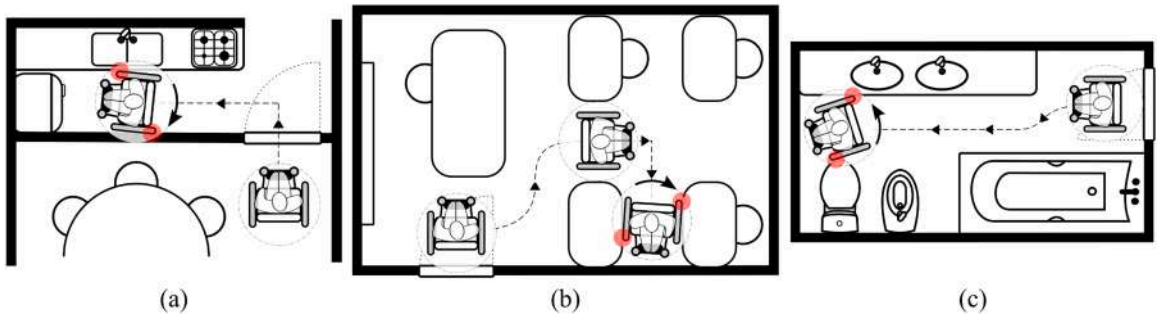

Fig. 2. Examples of critical situations of everyday wheelchair use in indoor environment: in red are highlighted the points where the wheelchair interferes with furniture: (a) navigation in a narrow kitchen corridor, (b) navigation in a classroom, (c) navigation in a bathroom. (For interpretation of the references to color in this figure legend, the reader is referred to the web version of this article.)

provided by passive caster wheels or, less frequently, omni-wheels. By controlling the velocity of the actuated wheels, it is possible to control the linear and angular velocity of the EPW, with the linear velocity vector always perpendicular to the traction wheels common axis, i.e., with the linear velocity vector aligned with the y-axis of reference $\{b\}$ in Fig. 1(a). Various wheel arrangements based on this locomotion principle are currently available on the market, as presented in Fig. 1(b)–(e).

Rear drive systems, Fig. 1(b), are usually characterized by good stability. However, they have a large turning radius due to the fact that the turning pivoting point is behind the user. Middle drive wheelchairs, Fig. 1(c), are more maneuverable in small spaces, but the four passive castor wheels may get stuck on uneven terrain. Front drive wheelchairs, Fig. 1(d), are typically slower but can achieve high stability on uneven terrain and on up hills, and therefore they are implemented mainly in outdoor applications, like four driven-wheels wheelchairs. This class of wheelchairs, Fig. 1(e), is designed to move on difficult terrains such as sand and snow. As a drawback, these wheelchairs are heavy, expensive, and require high maintenance. Because of their kinematic architecture (skid-steering system), their locomotion is modeled as an equivalent differential-drive system composed of two traction wheels mounted in the middle of the wheelchair, neglecting the wheel lateral skid while turning.

Regarding indoor applications, the major problem in EPWs adoption is related to the difficulty of navigating cluttered and confined environments. Conventional wheelchairs based on a differential-drive locomotion cannot move laterally. In other words, the instantaneous center of rotation always lies on the actuated wheels' common axis. This mobility limitation, coupled with architectural choices that fail to include wheelchair users in the building design process, often forces the user to perform numerous adjustment maneuvers or can ultimately impede their motion, as exemplified in some typical cases in Fig. 2.

To overcome the mobility limitations of conventional wheelchairs, several omnidirectional designs have been proposed in patent literature, academic research, and commercial sectors. Fig. 3 shows some examples of omnidirectional wheelchairs that had been proposed in the past. One prominent category utilizes omni-wheels or mecanum wheels [29–31]. These wheels feature passive rollers along their outer circumference, enabling free translation in directions perpendicular to the wheel's primary rotation. By integrating multiple wheels of this type, an omnidirectional base can be constructed. The absence of steering joints simplifies the mechanical

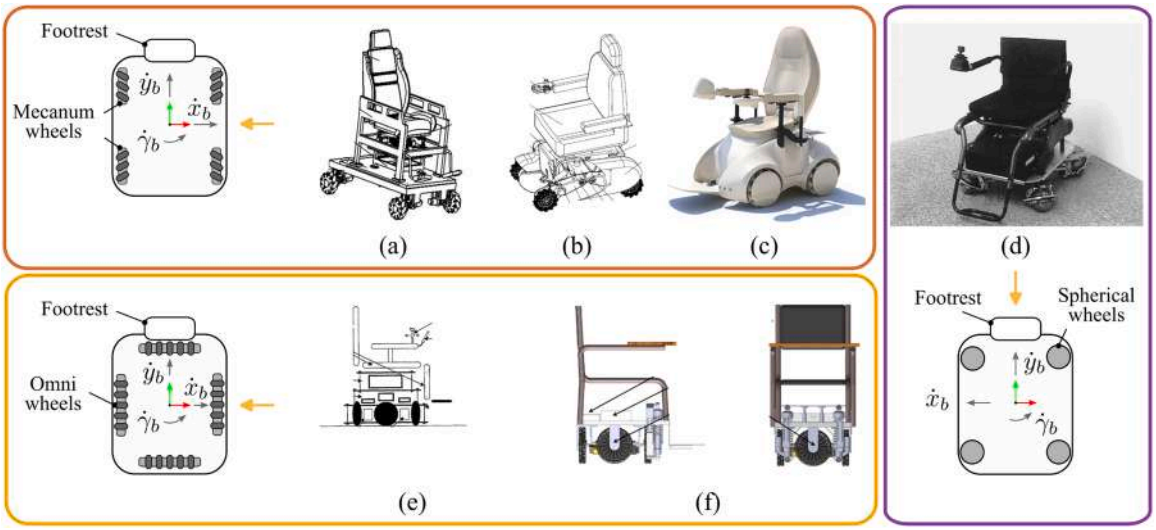

Fig. 3. Examples of omnidirectional electric-powered wheelchairs: (a) mecanum wheel EPW patent CN113440345A [34], (b) mecanum wheel EPW patent CN113440345A [34], (c) mecanum wheel EPW Omnichair by Omniroll [35], (d) spherical-wheel EPW by Wada et al. [33], (e) omni-wheel EPW patent ES2331554B1 [36], (f) omni-wheel EPW by Kundu et al. [29].

design, resulting in a level of complexity comparable to standard differential-drive systems. However, these solutions are significantly limited by the small diameter of the passive rollers, which reduces load capacity and diminishes user comfort. Furthermore, the discontinuous contact between these wheels and the ground induces vibrations and noise. The small rolling radius also increases sensitivity to ground irregularities and manufacturing tolerances, as detailed in [32].

A second category of omnidirectional EPWs employs spherical wheels, typically actuated by dual motors through an omni-chain transmission system or a cluster of omni-wheels [33]. These designs offer superior comfort and better adaptability to uneven terrain compared to mecanum or omni-wheel-based systems. Nevertheless, they are significantly more complex in both mechanical design and control logic. From a control perspective, these systems must maintain a normal force against the ground sufficient to generate the tangential forces required for propulsion. Furthermore, they must ensure that the normal forces between the omni-chain passive rollers and the spherical wheel are adequate to transmit power from the electric motors. Consequently, in critical scenarios such as navigating inclined ramps, the redistribution of normal loads could compromise the reliability of power transmission.

These inherent problems of existing omnidirectional EPWs likely explain why, despite being introduced in the late 1990s, these solutions have seen limited further development and have yet to result in viable commercial products.

Finally, the adoption of omnidirectional wheelchairs allows for a more efficient operational footprint, which can be approximated by the rectangle circumscribing the device. In contrast, the effective footprint of a conventional wheelchair is often overestimated as a circle centered at the midpoint of the actuated wheel axis. This overestimation is necessary to account for the space required for zero-radius turns. By eliminating the need for such wide clearance, omnidirectional systems reduce the stringent architectural constraints typically required for the design and adaptation of inclusive environments.

1.3. EPW drive interface state-of-the-art

The selection of a control interface for an electric-powered wheelchair depends on both the technical specifications of the device and the specific preferences of the user. These interfaces are generally classified into conventional joystick-based systems and alternative control methods. Joystick-based devices are the most widely utilized due to their intuitive operation and broad availability. To enhance accessibility and ergonomic fit, various handle configurations are available on the market, including soft-ball, T-handle, stick, dome, and U-shaped designs, as well as large-ball and chin-cup joysticks, as illustrated in Fig. 4. Significant research regarding the efficacy of these interfaces is provided in [37], which details a study involving interviews with twenty-two experienced power wheelchair users.

However, in cases where users cannot operate with conventional joysticks, alternative control solutions may be implemented. A comprehensive review by Ghorbel et al. (2019) [46] categorizes these alternative interfaces based on the input used:

- *EEG and ECG interfaces* exploit electro-biological signals to control EPWs [47–50]. These devices are based on Brain-Computer Interface (BCI) technology, which translates the measured signals into inputs for the wheelchair electronic control unit (example in Fig. 5(a)). Even if a good amount of research has already investigated the subject, this technology still has many drawbacks: complex treatment of EEC and ECG signals, error rate between 30% and 40%, and the possible dangerous implications on patients' health.



Fig. 4. Conventional joystick interfaces with different handles: (a) conventional joystick [38], (b) soft-ball handle [39], (c) T-handle [40], (d) stick joystick [41], (e) dome-shaped handles [42], (f) u-shaped handles [43], (g) large-ball handle [44], (h) chin cup joystick [45].

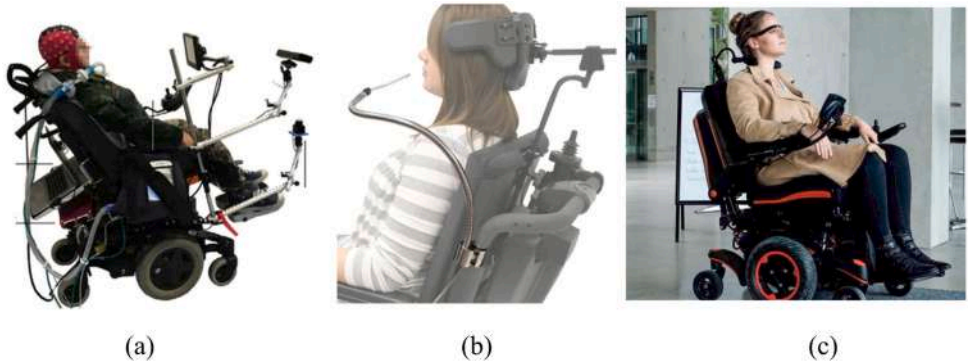

Fig. 5. Examples of alternative control interfaces: (a) brain-computer interface [50], (b) sip-and-puff system by Star Home Healthcare [51], (c) gaze tracking Munevo Drive system [61].

- *Sip-and-puff interfaces* are used by users to control the motion of the wheelchair by inhaling and exhaling into a sensorized straw [51,52] (example in Fig. 5(b)). The main advantage of this control interface is the ease of use, even if inhaling and exhaling can be tiring, and the straw must be cleaned frequently.
- *Voice-based interfaces* have been studied since the end of the '70s, and due to the robustness improvement of speech recognition techniques, they have been applied in many smart-wheelchairs projects, such as Scenario [53], NavChair [54] and MIT Wheelchair [55]. Even if this control interface can be used by people with average speech ability, the usability is strongly influenced by noise level, and communication is slow.
- *Tongue-based interfaces* are control interfaces that track the tongue's movement through the magnetic field measurements produced by a small magnet installed inside piercing [56]. Even if users with severe motor deficiency can use this technology, the approach is invasive and still just a research topic.
- *Head movement interfaces* recognize the position of the head using IMU sensors [57], or image recognition techniques [58] and translate this information into commands for the wheelchair. These control interfaces are cost-effective and non-invasive, but possible accidents may occur if the user turns his/her/their head to look around. To overcome this problem, the work [46] proposes an algorithm to classify actions into spontaneous and voluntary.
- *Gaze tracking interfaces* follow the eyes movements through image recognition techniques [59,60] (example in Fig. 5(c)). These systems are characterized by high sensitivity to light conditions and may lead to uncontrolled movements without proper classification algorithms.

In other cases, where users cannot drive the wheelchair independently, the wheelchair is provided with another driving interface that enables caregivers to drive the system. Usually, this additional driving interface is a commercial joystick mounted on the backrest; this setup is particularly adopted in wheelchairs for children. Even though this setup is quite simple and the joysticks are easily accessible, a problem may arise when a person not seated on the wheelchair commands the system with a joystick, as depicted in Fig. 6. First, the driver tilts the lever to increase the speed, then the system accelerates, but since the base of the joystick is fixed to the wheelchair, the tilt of the lever is reduced, and the system slows down.

To avoid this problem, much research has been conducted in the past on force-sensitive interfaces, exploring the possibility to replace rotations (the joystick tilt) with applied forces and torques. The underlying assumption is that it is easier to apply a constant force to a moving system rather than precisely control the angle of a lever when the base of the joystick is moving. Moreover, this type of interface mimics the way people move objects around. Based on experience, people apply forces and torque to obtain the desired motion. Therefore, with these interfaces a more intuitive interaction is expected. On force-sensitive interfaces, a force-velocity relationship has been proposed in [62] to obtain a controller that commands the wheelchair to accelerate if the attendant force exceeds a threshold value. This preliminary work considers no steering motion, and only simulation results are presented. In another work [63], Kakimoto et al. proposed a handlebar with a force sensor to assist caregivers in climbing ramps. In [64], the authors proposed a handlebar with a six-axis force sensor to measure force/torque inputs from the caregiver. Moreover, in the studies [65,66], advanced

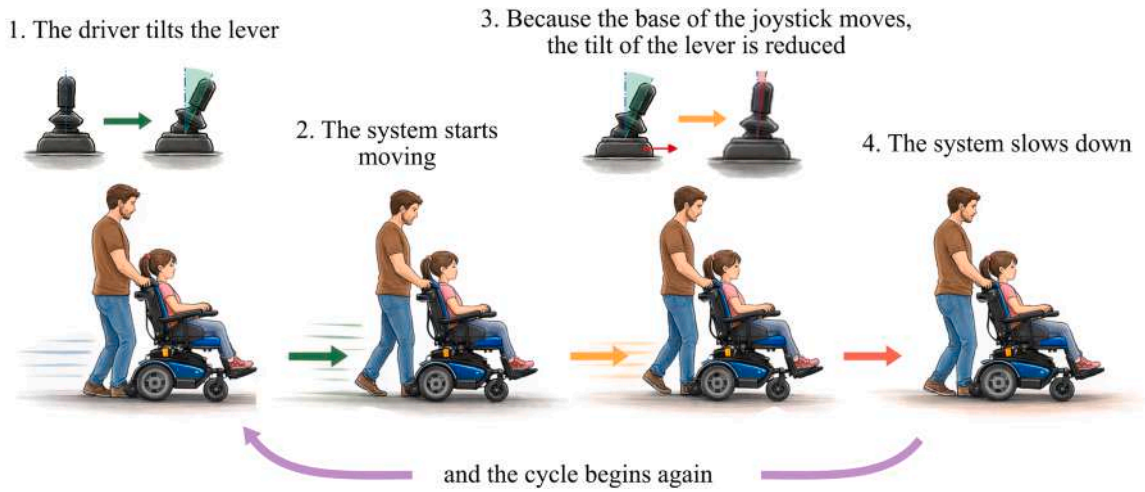

Fig. 6. Problem occurring when a person not seated on the wheelchair drives the system with a conventional joystick.

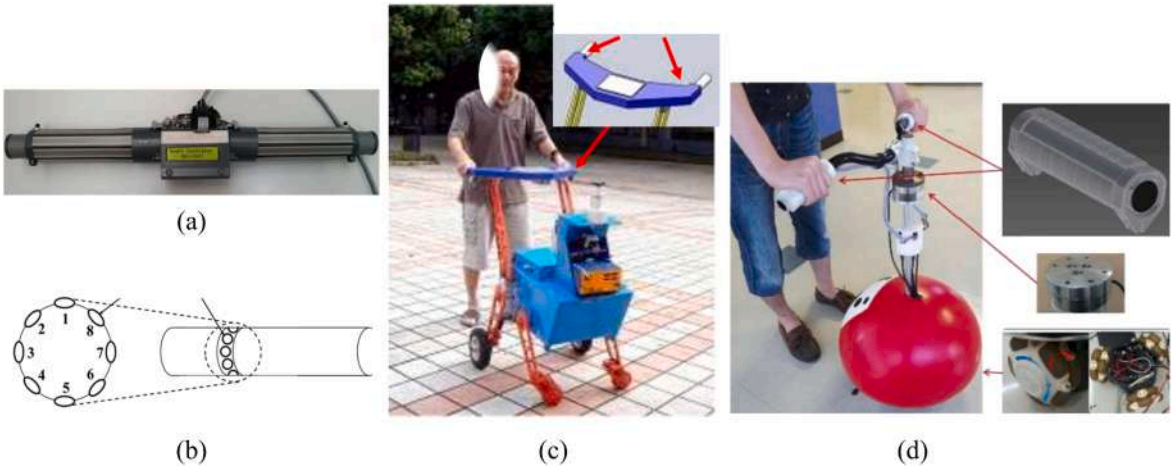

Fig. 7. Examples of sensorized handles conceived for caregivers: (a) tactile handlebar developed by Trujillo-León et al. [67], (b) sensorized handlebar for a walking assist system [68], (c) walking assistant robot with FSR in the handlebar [71], (d) grip sensor for a cane-type walking robot [72].

controllers have been proposed to improve the system's performance and cope with environmental disturbances. Another approach that has been adopted to build attendant handlebars makes use of tactile sensors, mainly FSR force sensing resistors [67–70]. The main advantages of this approach are: lower cost, they can be installed on ergonomic handles since they can be shaped into artificial skin. Conversely, the signals are more difficult to interpret, and often, the final inputs need better resolution. Fig. 7 shows some examples of the force-sensitive interfaces for caregivers.

1.4. Main contribution

The presented state-of-the-art analysis reveals two main limitations of current EPWs and drive interfaces:

1. the mobility limitation of conventional differential-drive wheelchairs is problematic during the navigation of spaces with obstacles and narrow passages. At the same time, omnidirectional EPWs based on mecanum wheels and omni wheels are characterized by high vibrations, high noise, low load capacity and reduced ability to deal with the presence of ground unevenness, while omnidirectional EPWs based on spherical wheels are more complex both in design and control.
2. research about drive interface for caregivers is not yet fully developed and suggests that improvements could enhance the cost-effectiveness of existing solutions. In fact, a subset of the current force-sensitive drive interfaces is not suitable for the control of omnidirectional systems, while other interfaces based on six-axis force-torque sensors could be adopted, but at a very high cost (six-axis force/torque sensors adopted in previous studies are notably expensive, in the range of €5000 to €12000 considering brands like BOTA SYTEMS, Kistler, and Futek).

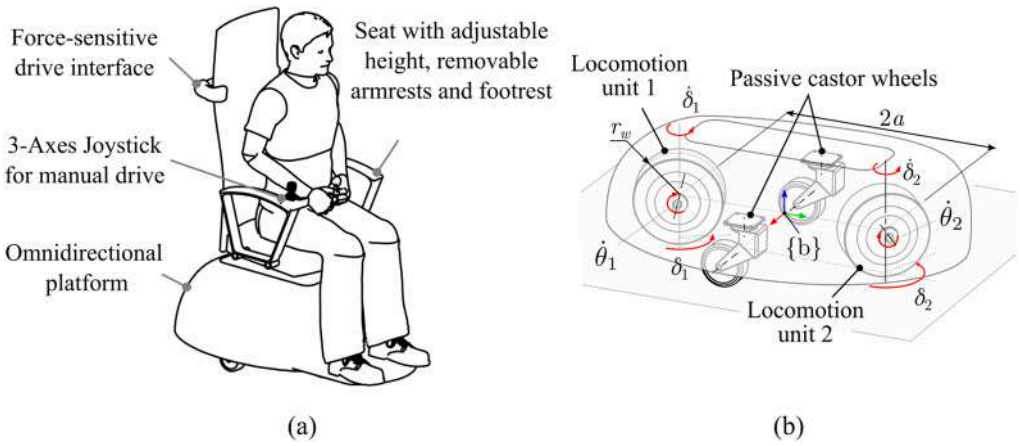

Fig. 8. (a) MoviWE.Q concept, (b) base platform locomotion system functional scheme.

Against this context, MoviWE.Q represents an innovative pseudo-omnidirectional swerve-drive electric powered wheelchair for indoor mobility. This EPW is conceived to overcome the mobility limitations of conventional differential-drive EPW, while at the same time improving the load-capacity and user comfort with respect to existing omnidirectional EPW based on special-wheels (spherical, omni-wheels and mecanum wheels). The technology is covered by the patent titled *Omnidirectional mobility device for people with reduced motorial function* (Priority Date: 27/10/2022, Priority Number: 102022000022155). To enable caregivers' intuitive drive mode, a custom designed force-sensitive drive interface, named SensHB.Q, is introduced. Then, experimental bench tests and laboratory test involving volounteers are presented to evaluate the performance of the EPW MoviWE.Q and the force-sensitive interface SensHB.Q.

This work builds on a few already published studies [73–75] and introduces the following novel contributions. With respect to [73] that just presents the concept of the EPW, this study details the development of the MoviWE.Q prototype, and introduces a detailed kinematic model of its locomotion system. The dimensionless approach presented in [75] for omnidirectional mobile robot is here applied to the wheelchair MoviWE.Q to study the achievable velocity twist given the wheel maximum speed. Another novel contribution is the kinematic analysis of the achievable velocity twist given the steering actuators maximum velocities. Then, the final prototype of SensHB.Q (with significant modifications with respect to [74]) is presented and bench tests have been reported to evaluate its accuracy. Finally, ISO 7176-5 tests and indoor navigation trials involving 18 volunteers driving MoviWE.Q using SensHB.Q are presented and discussed.

2. MoviWE.Q concept

Fig. 8(a) shows the concept of the device, composed of a seat with removable armrests, a footrest mechanism, a pseudo-omnidirectional mobile base platform, and control interfaces to drive the system. MoviWE.Q is conceived to be used in three drive modes:

- *Manual drive*: the user seated on the wheelchair commands the system through his/her preferred control interface, e.g., 3-axis joystick with conventional or unconventional handle. Alternative user interfaces may be adapted and integrated based on the user preferences (e.g., sip-and-puff interface, head movement interface).
- *Assisted drive*: caregivers can drive the wheelchair using a custom designed force-sensitive interface, named SensHB.Q, mounted on the backrest. The design and development of this interface is covered in Section 5.
- *Autonomous drive*: the wheelchair moves autonomously to the desired position, avoiding static and dynamic obstacles. This drive mode has been partially studied in previous research collaborations, but it goes out of the scope of this work that will focus on the first two drive modes only.

To overcome the limitations of both differential-drive locomotion and systems that rely on specially engineered wheels (e.g., mecanum, omni, or spherical wheels), MoviWE.Q is based on a pseudo-omnidirectional mobile base equipped with two swerve-drive locomotion units as depicted in Fig. 8(b). Each locomotion unit is composed of a motor wheel mounted on a vertical steering system that intersects the ground at the wheel-ground contact point. Two additional passive castor wheels are adopted to provide stability without the need for complex self-balancing systems. Here the term pseudo-omnidirectional mobility is used in accordance with Campion et al. ([76]) classification. The term "pseudo" refers to the fact that reorienting the wheels is necessary to achieve generic velocity twists.

To navigate in cluttered, tight spaces, a non-symmetric footprint is preferable to a symmetric one since the reduced size can be oriented to pass through confined spaces. As a downside, this non-symmetric and compact base leads to some challenges in terms of stability. Nevertheless, it must be underlined that MoviWE.Q is conceived for indoor use, with small maximum velocities and limited accelerations. Therefore, the inertial effects associated with rapid change in direction are limited.

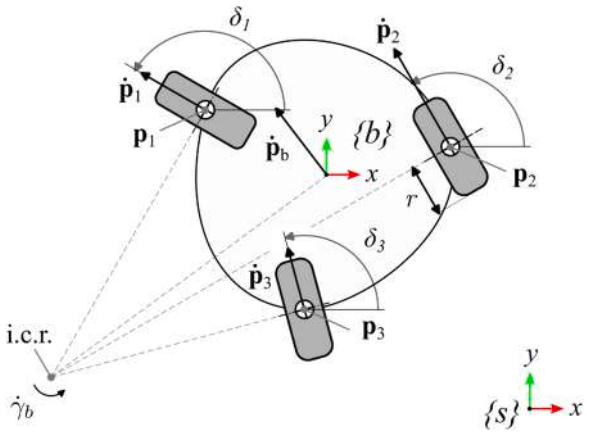

Fig. 9. Representation of a generic swerve drive system with $n = 3$ swerve-drive units.

To enable easy lateral and front access to the wheelchair, the system is provided respectively with removable armrests and a custom footrest mechanism. In particular, the footrest mechanism is designed to avoid interference with the feet during the opening/storage motion.

3. Kinematic model

Both in manual mode and autonomous mode, kinematic models of locomotion systems are essential to control the EPW motions. In fact, inverse kinematics is used to convert the desired velocity twist (composition of linear and angular velocity) into actuators commands, and all odometry estimations based on wheels feedback are based on forward kinematics. The kinematic models of wheeled mobile system have been deeply investigated in the past [76,77]. For swerve-drive locomotion system, the model is derived starting from the unicycle model. In Section 3.1, the kinematic model of swerve-drive-based platforms with n locomotion units is derived. This model is not a novel contribution of the paper, but it is essential for the subsequent analysis and it is useful to introduce the adopted nomenclature. Then, Section 3.2 adapts the generic formulation to the MoviWE.Q base platforms, while Section 3.3 and Section 3.4 explore the kinematic limitations of the system considering the actuators maximum speeds.

3.1. Kinematic model of swerve-drive-based platforms with n locomotion units

Let's consider a generic swerve-drive system composed of n swerve-drive units, as the one shown in Fig. 9. Each swerve-drive unit i is composed of a motor-wheel mounted on a vertical steering fork, that is actuated by means of a steering motor. Thus, each swerve-drive unit (also referred to as locomotion unit in this text) has two degrees of actuation: the wheel rotation θ_i around its own axis and the vertical steering angle δ_i. The wheel axis and the steering axis of each swerve-drive unit are incident, i.e., the wheel-ground contact point lies on the steering axis.

The system can be modeled as a rigid body in the plane of motion, that is considered parallel to the perfectly flat and smooth ground. If out of the plane rotations and translations are neglected, the body is free to move on the XY plane of the $\{s\}$ reference frame (rf). The pose of the body with respect to (wrt) the fixed-space frame $\{s\}$ is defined by the position vector ${}^s\mathbf{p}_b = [x, y, 0]^T$ and the vector of Euler angles (body-XYZ) $[0, 0, \gamma_b]^T$ equivalent to the orientation matrix ${}^sR_b = Rot(z, \gamma)$ that expresses the orientation of frame $\{b\}$ wrt frame $\{s\}$.

The space velocity twist of the system is defined as $\mathbf{V}_b^* = [\boldsymbol{\omega}_b, \dot{\mathbf{p}}_b]^T = [0, 0, \dot{\gamma}, \dot{x}, \dot{y}_b, 0]^T$, or in its three-dimensional form $\mathbf{V}_b = [\dot{\gamma}_b, \dot{x}_b, \dot{y}_b]^T$. The velocity twist and its time derivative can be expressed wrt frame $\{s\}$ or frame $\{b\}$, e.g., ${}^s\mathbf{V}_b = {}^s[\dot{\gamma}_b, \dot{x}_b, \dot{y}_b]^T$ and ${}^b\mathbf{V}_b = {}^b[\dot{\gamma}_b, \dot{x}_b, \dot{y}_b]^T$. Both ${}^s\mathbf{V}_b$ and ${}^b\mathbf{V}_b$ refer to the velocity twist of the body relative to the space frame $\{s\}$, but their components are expressed in two different reference frames. In this model, the goal is to derive the relationship between the space velocity twist ${}^b\mathbf{V}_b$ expressed relative to the body frame $\{b\}$ and the actuation vector $\mathbf{q} = [\mathbf{q}_1^T, \mathbf{q}_2^T, \dots, \mathbf{q}_n^T]^T$, where $\mathbf{q}_i = [\dot{\theta}_i, \delta_i]^T$.

The position of the center of the generic locomotion unit i wrt the body frame $\{b\}$ is described by the two-dimensional vector $\mathbf{p}_i = [x_i, y_i]^T$. This point is considered the attachment point of the swerve-drive unit to the system chassis. Under the assumption of rigid body, the velocity $\dot{\mathbf{p}}_i$ of the center points of the locomotion unit i can be evaluated using (1).

$$\begin{bmatrix}\dot{\mathbf{p}}_i\\0\end{bmatrix} = \begin{bmatrix}\dot{\mathbf{p}}\\0\end{bmatrix} + \begin{bmatrix}0\\0\\\dot{\gamma}_b\end{bmatrix} \times \begin{bmatrix}\mathbf{p}_i\\0\end{bmatrix} \quad \Leftrightarrow \quad \dot{\mathbf{p}}_i = \begin{bmatrix}-y_i & 1 & 0\\ x_i & 0 & 1\end{bmatrix}\mathbf{V}_b = H_i\mathbf{V}_b \tag{1}$$

At the same time, under the assumption of pure-rolling constraint, the velocity of the center points of the locomotion unit i can be evaluated as in (2).

$$\dot{\mathbf{p}}_i = r_i \begin{bmatrix} c_{\delta_i} \\ s_{\delta_i} \end{bmatrix} \dot{\theta}_i = \mathbf{s}_i \dot{\theta}_i \tag{2}$$

where $c_{\delta_i} = \cos(\delta_i)$ and $s_{\delta_i} = \sin(\delta_i)$ and r_i is the wheel radius. Given (1) and (2), the relationship between the body-velocity twist $\mathbf{V}_b$ and the wheel actuation variables of wheel ith is expressed by (3).

$$H_i \mathbf{V}_b = \mathbf{s}_i \dot{\theta}_i \qquad \text{where } H_i = \begin{bmatrix} -y_i & 1 & 0 \\ x_i & 0 & 1 \end{bmatrix}, \text{ and } \mathbf{s}_i = r_i \begin{bmatrix} c_{\delta_i} \\ s_{\delta_i} \end{bmatrix} \tag{3}$$

Then, if all locomotion units are considered, (4) express the relationship between the body-velocity twist $\mathbf{V}_b$ and the four actuation variables θ_i, δ_i $(i = 1, \dots, n)$.

$$\begin{bmatrix} H_1 \\ H_2 \\ \vdots \\ H_n \end{bmatrix} \mathbf{V}_b = \begin{bmatrix} \mathbf{s}_1 & 0 & \dots & 0 \\ 0 & \mathbf{s}_2 & \dots & 0 \\ \vdots & \vdots & \ddots & \vdots \\ 0 & 0 & \dots & \mathbf{s}_n \end{bmatrix} \begin{bmatrix} \dot{\theta}_1 \\ \dot{\theta}_2 \\ \vdots \\ \dot{\theta}_n \end{bmatrix} \qquad \Leftrightarrow \qquad H \mathbf{V}_b = S(\boldsymbol{\delta}) \dot{\boldsymbol{\theta}} \tag{4}$$

where $\boldsymbol{\delta} = [\delta_1, \delta_2, \dots, \delta_n]^T$ and $\dot{\boldsymbol{\theta}} = [\dot{\theta}_1, \dot{\theta}_2, \dots, \dot{\theta}_n]^T$. The matrix H depends only on the location of the swerve-drive units wrt the $\{b\}$ frame, while the matrix $S(\boldsymbol{\delta})$ is state-dependent. In fact, for swerve-drive systems, it is impossible to derive a linear transformation that maps the actuation vector $\mathbf{q}$ into the velocity twist of the system $\mathbf{V}_b$. The matrix H is a $2n \times 3$ matrix, while the S matrix is a $2n \times n$ matrix.

The system has three degrees of freedom and $2n$ actuation variables. Let's imagine that each locomotion unit has a unique position vector, then for $n \geq 2$ the system has $2n - 3$ actuation redundancy. Therefore, an arbitrary choice of the actuation variables could result in skidding of the wheels. The actuation variables must be chosen on a three-dimensional surface in the $2n$ dimensional actuation space. For this reason, a set of $2n - 3$ constraints must be fulfilled to avoid skidding of the wheels. This set of kinematic constraints is defined by (5).

$$\dot{\mathbf{p}}_i^T (\mathbf{p}_i - \mathbf{p}_j) = \dot{\mathbf{p}}_j^T (\mathbf{p}_i - \mathbf{p}_j) \Leftrightarrow ((x_i - x_j) c_{\delta_i} + (y_i - y_j) s_{\delta_i}) \dot{\theta}_i = ((x_i - x_j) c_{\delta_j} + (y_i - y_j) s_{\delta_j}) \dot{\theta}_j \quad (\forall\, i \neq j) \tag{5}$$

In other words, the velocity components of the center of two swerve-drive units in the direction that connects the two centers of the two swerve-drive units must be equal, i.e., the assumption of rigid body must be fulfilled.

If the actuation variables are such that the kinematic constraint (5) is fulfilled, the body-velocity twist can be computed from the actuation variable using the velocity forward kinematics expressed by (6). This relationship can be easily derived from (4) using the pseudo-inverse matrix $H^\dagger$ of matrix H.

$$\mathbf{V}_b = H^\dagger S(\boldsymbol{\delta}) \dot{\boldsymbol{\theta}} \tag{6}$$

Regarding the velocity inverse kinematics, the same approach is not useful since the matrix $S(\boldsymbol{\delta})$ is state-dependent. A practical way to solve the inverse kinematics of the system is to consider each locomotion unit independently. Given the desired velocity twist $\mathbf{V}_b$, the velocity $\dot{\mathbf{p}}_i$ of point $\mathbf{p}_i$ can be evaluated through (1). The norm of the velocity vector can be computed as $\|\dot{\mathbf{p}}_i\| = \sqrt{\dot{\mathbf{p}}_i^T \dot{\mathbf{p}}_i}$ and, therefore, the actuation variables associated to the locomotion unit i can be evaluated as in (7).

$$\begin{cases} \delta_i &= \text{atan2}(\dot{y}_i / \|\dot{\mathbf{p}}_i\|,\, \dot{x}_i / \|\dot{\mathbf{p}}_i\|) + k\pi \\ \dot{\theta}_i &= (-1)^k \|\dot{\mathbf{p}}_i\| / r_i \end{cases} \qquad \text{where } k \in \mathbb{Z} \tag{7}$$

Thus, for $\delta_i \in [-\pi, \pi]$, there are two possible solutions to the inverse kinematic problem for each swerve-drive system. This is in accordance with the physics of the system: the velocity of the center of the wheel is the same if the wheel turns π around the vertical steering axis, and it spins in the opposite direction.

3.2. Kinematic model applied to MoviWE.Q

This section applies the kinematic model presented in Section 3.1 to the proposed pseudo-omnidirectional EPW. MoviWE.Q is composed of two swerve-drive units ($n = 2$), and the $\{b\}$ frame is placed at the intersection point between the segment connecting the traction wheel attachment points ($\mathbf{p}_1$, $\mathbf{p}_2$) and the castor wheel attachment points. Considering the 3D functional scheme presented in Fig. 8(b) and its planar version in Fig. 10(a), the traction wheel attachment points are defined as in (8).

$$\mathbf{p}_1 = \begin{bmatrix} 0 & -a \end{bmatrix}^T; \qquad \mathbf{p}_2 = \begin{bmatrix} 0 & a \end{bmatrix}^T \tag{8}$$

Using Eq. (1), it is possible to derive the relationship between the platform velocity twist $\mathbf{V}_b$ and the linear velocity of the traction wheel attachment points, as show in (9)

$$\dot{\mathbf{p}}_1 = \begin{bmatrix} a & 1 & 0 \\ 0 & 0 & 1 \end{bmatrix} \mathbf{V}_b = \begin{bmatrix} \dot{x}_b + a\dot{\gamma}_b \\ \dot{y}_b \end{bmatrix}; \qquad \dot{\mathbf{p}}_2 = \begin{bmatrix} -a & 1 & 0 \\ 0 & 0 & 1 \end{bmatrix} \mathbf{V}_b = \begin{bmatrix} \dot{x}_b - a\dot{\gamma}_b \\ \dot{y}_b \end{bmatrix} \tag{9}$$

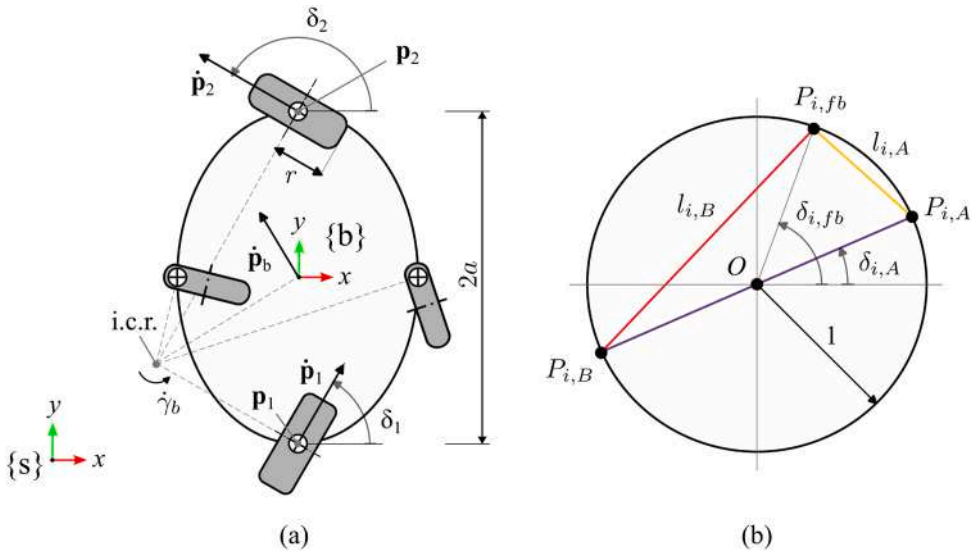

Fig. 10. (a) 2D functional scheme of MoviWE.Q locomotion system; (b) unit circle and geometric parameter definition for the selection of the inverse kinematic solution that minimizes the steering rotation for the locomotion unit i.

Assuming that $r_1 = r_2 = r$ is the traction wheel radius, the velocity forward kinematic relationship can be derived from (6), and written as in (10).

$$\mathbf{V}_b = H^{\dagger} S(\boldsymbol{\delta})\dot{\boldsymbol{\theta}} = \frac{r}{a}\begin{bmatrix} 1/2 & 0 & -1/2 & 0 \\ a/2 & 0 & a/2 & 0 \\ 0 & a/2 & 0 & a/2 \end{bmatrix}\begin{bmatrix} c_{\delta_1} & 0 \\ s_{\delta_1} & 0 \\ 0 & c_{\delta_2} \\ 0 & s_{\delta_2} \end{bmatrix}\begin{bmatrix} \dot{\theta}_1 \\ \dot{\theta}_2 \end{bmatrix} = \frac{r}{2}\begin{bmatrix} \frac{1}{a}\left(c_{\delta_1}\dot{\theta}_1 - c_{\delta_2}\dot{\theta}_2\right) \\ c_{\delta_1}\dot{\theta}_1 + c_{\delta_2}\dot{\theta}_2 \\ s_{\delta_1}\dot{\theta}_1 + s_{\delta_2}\dot{\theta}_2 \end{bmatrix} \tag{10}$$

Using Eq. (10) it is possible to compute the platform velocity twist from the actuation variables $\dot{\theta}_1$, $\dot{\theta}_2$, δ_1 and δ_2, if and only if the actuation variables are chosen on a three-dimensional surface in the four-dimensional actuation space such that pure rolling constraint is satisfied. In this case, considering generic traction wheel velocity vectors from (2), the kinematic constraint (5) among the actuation variables can be written as in (11).

$$\dot{\mathbf{p}}_i^T(\mathbf{p}_i - \mathbf{p}_j) = \dot{\mathbf{p}}_j^T(\mathbf{p}_i - \mathbf{p}_j) \qquad \Leftrightarrow \qquad s_{\delta_1}\dot{\theta}_1 = s_{\delta_2}\dot{\theta}_2 \tag{11}$$

Regarding the velocity inverse kinematics, given the desired velocity twist $\mathbf{V}_b$, the actuation variables can be computed using Eq. (12) and (13), derived from (7).

$$\begin{cases} \delta_1 &= \operatorname{atan2}\left(\dot{y}_b/\|\dot{\mathbf{p}}_1\|, (\dot{x}_b + a\dot{\gamma}_b)/\|\dot{\mathbf{p}}_1\|\right) + k\pi \\ \dot{\theta}_1 &= (-1)^k\|\dot{\mathbf{p}}_1\|/r_i \end{cases} \quad \text{where } k \in \mathbb{Z};\ \text{and } \|\dot{\mathbf{p}}_1\| = \sqrt{(\dot{x}_b + a\dot{\gamma}_b)^2 + (\dot{y}_b)^2} \tag{12}$$

$$\begin{cases} \delta_2 &= \operatorname{atan2}\left(\dot{y}_b/\|\dot{\mathbf{p}}_2\|, (\dot{x}_b - a\dot{\gamma}_b)/\|\dot{\mathbf{p}}_2\|\right) + k\pi \\ \dot{\theta}_2 &= (-1)^k\|\dot{\mathbf{p}}_2\|/r_i \end{cases} \quad \text{where } k \in \mathbb{Z};\ \text{and } \|\dot{\mathbf{p}}_2\| = \sqrt{(\dot{x}_b - a\dot{\gamma}_b)^2 + (\dot{y}_b)^2} \tag{13}$$

Thus, for $\delta_i \in [-\pi, \pi]$, there are two possible solutions to the inverse kinematic problem for each swerve-drive system ($\delta_{i,A}$, $\dot{\theta}_{i,A}$, $\delta_{i,B}$, $\dot{\theta}_{i,B}$) for a total of four independent solutions of the velocity inverse kinematic problem. In practical applications, given the current state of the steering joint $\delta_{i,fb}$, the most common choice for the inverse kinematic solution selection between $\delta_{i,A}$ and $\delta_{i,B}$ is to choose the solution that minimize the steering angular distance. In many applications, multi turns steering system are adopted, and this is the case for MoviWE.Q. Therefore, the evaluation of the minimum angular distance must consider multi turns. A practical way to address the problem is to compare the chord lengths $l_{i,A}$ and $l_{i,B}$, as shown in Fig. 10(b). The points $P_{i,fb}$, $P_{i,A}$, and $P_{i,B}$ lie on a unit circumference. The chord lengths $l_{i,A}$ and $l_{i,B}$ can be computed as in (14) and (15).

$$l_{i,A} = \sqrt{(c_{\delta_{i,fb}} - c_{\delta_{i,A}})^2 + (s_{\delta_{i,fb}} - s_{\delta_{i,A}})^2} = \sqrt{2(1 - \cos(\delta_{i,fb} - \delta_{i,A}))} \tag{14}$$

$$l_{i,B} = \sqrt{(c_{\delta_{i,fb}} - c_{\delta_{i,B}})^2 + (s_{\delta_{i,fb}} - s_{\delta_{i,B}})^2} = \sqrt{2(1 - \cos(\delta_{i,fb} - \delta_{i,B}))} \tag{15}$$

Thus, the inverse kinematic computation can be summarized as in Algorithm 1.

Algorithm 1 Actuation variables computation algorithm.

for all $i = 1, 2$ **do**
  $\dot{\theta}_{i,A} = \|\dot{\mathbf{p}}_i\|/r$; $\quad \dot{\theta}_{i,B} = -\dot{\theta}_{i,A}$;
  $\delta_{i,A} = \text{atan2}(\dot{y}_i, \dot{x}_i)$; $\quad \delta_{i,B} = \text{wrapToPi}(\delta_{i,A} + \pi)$;
  if $\left(\sqrt{2(1-\cos(\delta_{i,fb} - \delta_{i,A}))} \leq \sqrt{2(1-\cos(\delta_{i,fb} - \delta_{i,B}))}\right)$ **then**
    $\delta_i = \delta_{i,A}$; $\quad \dot{\theta}_i = \dot{\theta}_{i,A}$;
  else
    $\delta_i = \delta_{i,B}$; $\quad \dot{\theta}_i = \dot{\theta}_{i,B}$;
  end if
end for

3.3. Velocity twist limits given the maximum wheel velocity

This section investigates how the maximum wheel speed affects the achievable system velocity twist. To evaluate the systemic influence of the maximum wheel angular velocity on the body velocity twist $\mathbf{V}_b$ within a given locomotion architecture, a dimensionless formulation is adopted. This approach follows the methodology detailed by the authors in a previous study [75], which compared two omnidirectional locomotion strategies for mobile robots (mecanum wheel and omniwheel based robots) to a pseudo-omnidirectional swerve-drive-based platform.

The dimensionless linear velocities are defined as $\dot{X}_b = \dot{x}_b/(r\,\dot{\theta}_{\max})$ and $\dot{Y}_b = \dot{y}_b/(r\,\dot{\theta}_{\max})$, while the dimensionless yaw angular rate is expressed as $\dot{\Gamma}_b = (a\,\dot{\gamma}_b)/(r\,\dot{\theta}_{\max})$. To complete this normalized framework, the dimensionless wheel angular velocity for the ith wheel is defined as $\Omega_i = \dot{\theta}_i/\dot{\theta}_{\max}$.

In physical platforms, the angular velocity of each traction wheel i is constrained by the actuator limit $|\dot{\theta}_i| \leq \dot{\theta}_{\max}$, which corresponds to the dimensionless bound $|\Omega_i| \leq 1$ (i.e., $-1 \leq \Omega_i \leq 1$). Fig. 11(a) illustrates the permissible dimensionless body twist space for a two-swerve-drive-unit locomotion system. The complete set of feasible dimensionless body twists $[\dot{\Gamma}_b\ \dot{X}_b, \dot{Y}_b]^T$ must reside within this workspace volume. Fig. 11(b), (c), and (d) depict the respective cross-sections of this permissible space taken along the planes $\dot{X}_b = c$, $\dot{Y}_b = c$, and $\dot{\Gamma}_b = c$, where $c \in [0, 1]$.

The allowed dimensionless body twist space forms a specific geometric solid characterized by unit circular cross-sections on the $\dot{X}_b = 0$ and $\dot{\Gamma}_b = 0$ planes, and a unit square cross-section on the $\dot{Y}_b = 0$ plane. This velocity limitation associated with the longitudinal speed $\dot{X}_b$ arises because, while the platform moves in the x direction, a yaw angular rate can only be achieved via a differential-drive strategy. Consequently, the outer wheel (with respect to the turn maneuver) reaches its maximum speed limit at values of $\dot{X}_b$ and $\dot{\Gamma}_b$ strictly lower than 1. Conversely, when the platform translates along the y direction, the yaw angular rate is generated by exploiting the steering degrees of actuation, thereby avoiding the kinematic limitations associated with differential-drive steering.

This dimensionless analysis also highlights the critical influence of the system's geometric parameters. An increase in the wheel radius r yields a proportional increase in the maximum allowable velocity across all directions. Conversely, an increase in the geometric parameter a results in a contraction of the allowed velocity space along the $\dot{\Gamma}_b$ axis.

Numerical results can be computed once the wheel radius r, the geometric parameter a, and the maximum wheel speed $\dot{\theta}_{\max}$ are defined. For MoviWE.Q, these values are $r = 101$ mm, $a = 250$ mm, and $\dot{\theta}_{\max} = 200$ rpm. Consequently, the allowed velocity space and its cross-sections are shown in Fig. 12. The maximum magnitude of the linear velocity vector is $\|\dot{\mathbf{p}}_b\| = 2.12$ m/s, and this velocity vector can be oriented in any direction within the $\dot{\gamma}_b = 0$ plane. The maximum absolute value of the yaw angular rate is $\dot{\gamma}_b = 8.46$ rad/s, which can be achieved when $\|\dot{\mathbf{p}}_b\| = 0$ m/s. It should be clarified that these maximum values of the velocity twist components are way above the suited maximum linear and yaw angular velocity for an indoor EPW like MoviWE.Q.

3.4. Minimum curvature radius given the maximum steering velocity

Section 3.3 investigated the influence of the traction wheels' maximum angular speed on the allowed body velocity twist of the system. However, physical platforms based on swerve-drive locomotion are constrained by both maximum traction wheel speeds and maximum steering axis velocities. This section investigates how the maximum steering velocity $\dot{\delta}_{\max}$ influences the system's motion capabilities. The actuation variables δ_1, δ_2, $\dot{\theta}_1$, and $\dot{\theta}_2$ define the body velocity twist of the system and are subjected to the kinematic constraints (11). Correspondingly, the body acceleration twist is governed by the steering velocities $\dot{\delta}_1$ and $\dot{\delta}_2$, the traction wheel accelerations $\ddot{\theta}_1$ and $\ddot{\theta}_2$, as well as the current state variables δ_1, δ_2, $\dot{\theta}_1$, and $\dot{\theta}_2$. By taking the time derivative of (10), the body acceleration twist $\dot{\mathbf{V}}_b$ is obtained as shown in (16). Consequently, the steering velocities $\dot{\delta}_1$, $\dot{\delta}_2$ and traction wheel accelerations $\ddot{\theta}_1$, $\ddot{\theta}_2$ directly dictate the rate of change of the system's velocity twist, thereby defining the range of achievable dynamic maneuvers.

$$\dot{\mathbf{V}}_b = \begin{bmatrix} \ddot{\gamma}_b \\ \ddot{x}_b \\ \ddot{y}_b \end{bmatrix} = \frac{r}{2} \begin{bmatrix} \frac{1}{a}\left(\ddot{\theta}_1 c_{\delta_1} - \dot{\theta}_1 \dot{\delta}_1 s_{\delta_1} - \ddot{\theta}_2 c_{\delta_2} + \dot{\theta}_2 \dot{\delta}_2 s_{\delta_2}\right) \\ \ddot{\theta}_1 c_{\delta_1} - \dot{\theta}_1 \dot{\delta}_1 s_{\delta_1} + \ddot{\theta}_2 c_{\delta_2} - \dot{\theta}_2 \dot{\delta}_2 s_{\delta_2} \\ \ddot{\theta}_1 s_{\delta_1} + \dot{\theta}_1 \dot{\delta}_1 c_{\delta_1} + \ddot{\theta}_2 s_{\delta_2} + \dot{\theta}_2 \dot{\delta}_2 c_{\delta_2} \end{bmatrix} \tag{16}$$

In real systems based on swerve-drive locomotion the steering axis velocities represents the main limitations. The maximum steering velocity $\dot{\delta}_{\max}$ has a major impact on the achievable trajectory curvature radius r_{curv}.

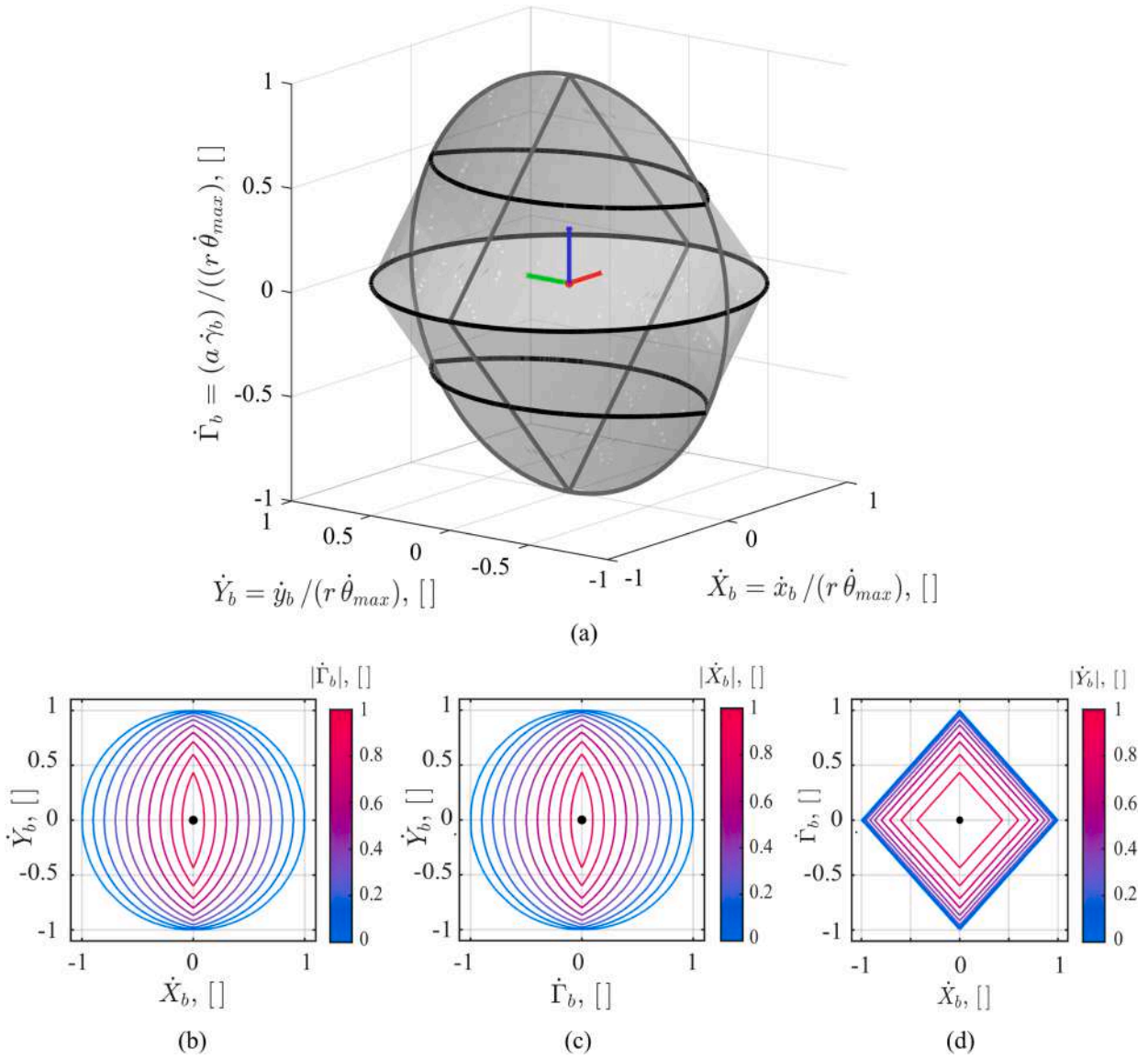

Fig. 11. (a) allowed dimensionless body twist space for a two swerve-drive-units mobile system; (b) cross-sections of the allowed dimensionless body twist space in (a) with planes $\dot{\Gamma}_b = c$ ($c \in [0, 1]$); (c) cross-sections of the allowed dimensionless body twist space in (a) with planes $\dot{X}_b = c$ ($c \in [0, 1]$); (d) cross-sections of the allowed dimensionless body twist space in (a) with planes $\dot{Y}_b = c$ ($c \in [0, 1]$).

In general, given the system linear velocity and acceleration vectors $\dot{\mathbf{p}}_b = \begin{bmatrix}\dot{x}_b & \dot{y}_b & 0\end{bmatrix}^T$, and $\ddot{\mathbf{p}}_b = \begin{bmatrix}\ddot{x}_b & \ddot{y}_b & 0\end{bmatrix}^T$, the point $\mathbf{p}_b$ trajectory tangent and normal unit vectors (respectively $\hat{\mathbf{t}}$ and $\hat{\mathbf{n}}$) are defined as in (17).

$$\hat{\mathbf{t}} = \frac{\dot{\mathbf{p}}_b}{\|\dot{\mathbf{p}}_b\|}; \qquad \hat{\mathbf{n}} = \begin{bmatrix}0\\0\\1\end{bmatrix} \times \hat{\mathbf{t}} \tag{17}$$

Therefore, the absolute value of the centripetal acceleration a_c of the system can be derived as the component of the acceleration on the normal unit vector $\hat{\mathbf{n}}$, as in (18).

$$a_c = \|\ddot{\mathbf{p}}_b^T \hat{\mathbf{n}}\| = \frac{|\dot{y}_b \dot{x}_b - \ddot{x}_b \dot{y}_b|}{\|\dot{\mathbf{p}}_b\|} \tag{18}$$

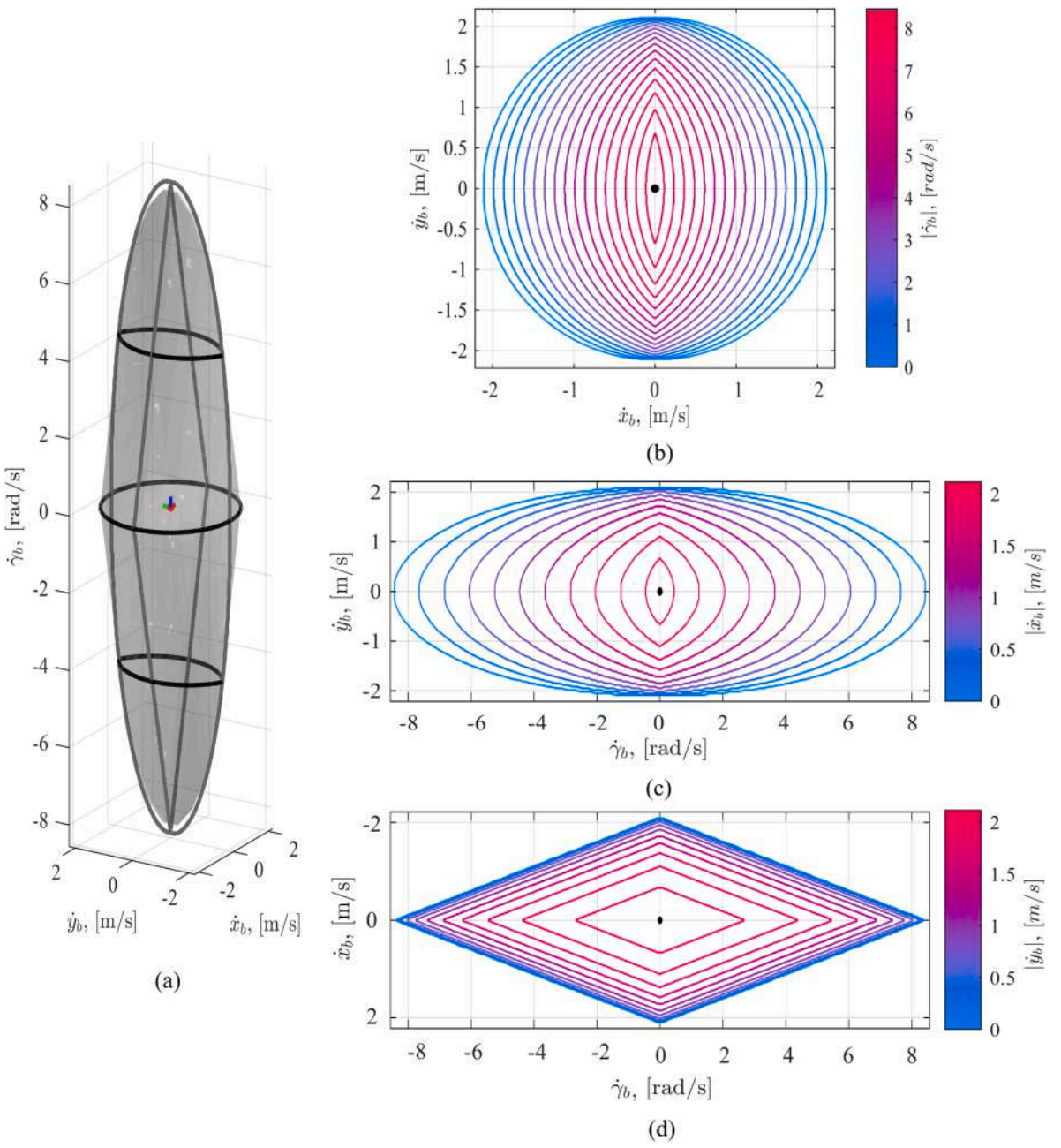

Fig. 12. (a) allowed body twist space for MoviWE.Q; (b) cross-sections of the allowed body twist space in (a) with planes $\dot{\gamma}_b = c$ ($c \in [0, \dot{\gamma}_{\max}]$); (c) cross-sections of the allowed body twist space in (a) with planes $\dot{x}_b = c$ ($c \in [0, \dot{x}_{\max}]$); (d) cross-sections of the allowed body twist space in (a) with planes $\dot{x}_b = c$ ($c \in [0, \dot{x}_{\max}]$).

Which lead to the computation of the instantaneous curvature radius r_{curv} as in (19).

$$r_{curv} = \frac{\|\dot{\mathbf{p}}_b\|^2}{a_c} = \frac{\|\dot{\mathbf{p}}_b\|^3}{|\ddot{y}_b\dot{x}_b - \ddot{x}_b\dot{y}_b|} = r_{curv}(\delta_1, \delta_2, \dot{\theta}_1, \dot{\theta}_2, \dot{\delta}_1, \dot{\delta}_2, \ddot{\theta}_1, \ddot{\theta}_2) =$$
$$= \frac{r}{2} \frac{\left(A^2 + B^2\right)\sqrt{\left|\dot{\theta}_1^2 + \dot{\theta}_2^2 + 2\dot{\theta}_1\dot{\theta}_2 c_{\delta_1-\delta_2}\right|}}{\left|\dot{\delta}_1\dot{\theta}_1^2 + \dot{\delta}_2\dot{\theta}_2^2 - \dot{\theta}_1\ddot{\theta}_2 s_{\delta_1-\delta_2} + \dot{\theta}_2\ddot{\theta}_1 s_{\delta_1-\delta_2} + \dot{\delta}_1\dot{\theta}_1\dot{\theta}_2 c_{\delta_1-\delta_2} + \dot{\delta}_2\dot{\theta}_1\dot{\theta}_2 c_{\delta_1-\delta_2}\right|} \tag{19}$$

where $A = \dot{\theta}_1 s_{\delta_1} + \dot{\theta}_2 s_{\delta_2}$, $B = \dot{\theta}_1 c_{\delta_1} + \dot{\theta}_2 c_{\delta_2}$, $c_{\delta_1-\delta_2} = \cos(\delta_1 - \delta_2)$, and $s_{\delta_1-\delta_2} = \sin(\delta_1 - \delta_2)$. From (19), it is difficult to directly isolate the influence of the maximum actuation velocity and acceleration limits on the resulting motion. However, practical insights can

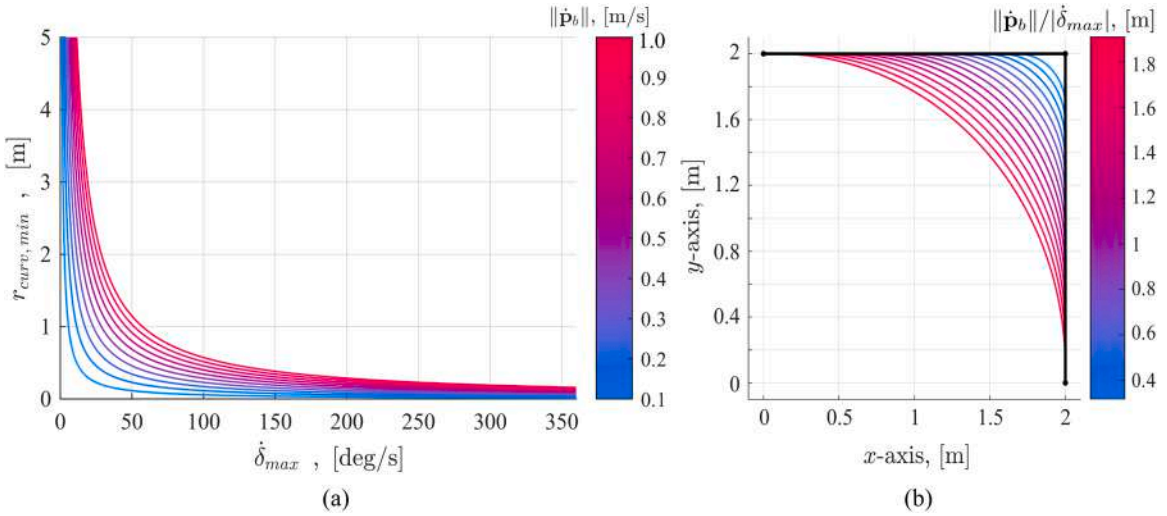

Fig. 13. (a) relationship between $\dot{\delta}_{\max}$ and $r_{curv,min}$ for different linear velocity module $\|\dot{\mathbf{p}}_b\|$; (b) trajectories of minimum radius to approximate a sharp corner trajectory (black line) given the ratio $\|\dot{\mathbf{p}}_b\|/|\dot{\delta}_{\max}|$.

be gained by considering a pure translational motion (i.e., $\dot{\gamma}_b = 0$ rad/s) at a constant linear velocity magnitude (i.e., $\|\dot{\mathbf{p}}_b\| = \text{const}$). Under these conditions, the velocity inverse kinematics (12) and (13) yield $\delta_1 = \delta_2 = \delta$ and $\dot{\theta}_1 = \dot{\theta}_2 = \dot{\theta}$, while the wheel accelerations vanish ($\ddot{\theta}_1 = \ddot{\theta}_2 = 0$ rad/s^2). Assuming $\dot{\delta}_1 = \dot{\delta}_2 = \dot{\delta}$, Eq. (19) simplifies significantly to (20).

$$r_{curv} = \frac{\|\dot{\mathbf{p}}_b\|}{|\dot{\delta}|}; \quad \Rightarrow \quad r_{curv,min} = \frac{\|\dot{\mathbf{p}}_b\|}{|\dot{\delta}_{max}|} \tag{20}$$

The relationship between the maximum steering velocity $\dot{\delta}_{\max}$ and the minimum curvature radius $r_{curv,min}$ for a given linear velocity magnitude is depicted in Fig. 13(a). This relationship can also serve as a design tool to evaluate the required maximum steering velocity for a specified minimum curvature radius at a given operational speed. The practical implications of this constraint are illustrated in Fig. 13(b). If a sharp-corner trajectory (indicated by the black line in Fig. 13(b)) is commanded, the physical system will approximate the discontinuity with a filet. The minimum radius of this achievable path is defined by the ratio $\|\dot{\mathbf{p}}_b\|/|\dot{\delta}_{\max}|$. From (20), it is clear that the wheelchair can still perform sharp corner trajectories, but it needs to stop at the corner and reorient the wheels.

4. Prototype

4.1. Overall dimensions and specifications

This section presents the mechanical design of MoviWE.Q. Firstly, an overview of the final design is provided, and then the main sub-assemblies are discussed individually. Fig. 14 depicts the MoviWE.Q prototype. The wheelchair footprint can be approximated with a rectangle of sides 630×700 mm when the footrest is closed (630×990 mm when the footrest is opened). The seat height from the ground is around 550 mm, and it can be adjusted between 500 mm and 600 mm. The base platform is mainly made of aluminum tubes and clamps and 3D-printed components for the non-structural parts for a total weight of about 36 kg (without the battery that weighs around 5.0 kg).

Regarding the mechanical structure of MoviWE.Q, the main sub-assemblies are the two locomotion units, the chassis, the two castor wheels, the seat, and the footrest mechanism.

4.2. Subsystems in detail

From a mechanical design perspective, the most complex subsystem of the platform is the locomotion unit, which has been developed as an integrated assembly. Each locomotion unit comprises a commercial motor-wheel mounted within a custom steering system, as illustrated in Fig. 15. The motor-wheel is an 8-inch, low-speed hub motor featuring a non-marking tire, manufactured by UU Motor Technology Co. This motor-wheel integrates a brushless motor operating at 24 V, capable of delivering a maximum speed of 200 rpm, rated torque 20 Nm, and peak torque 40 Nm, and Hall-effect sensors for measuring wheel angular velocity. The component is characterized by an outer diameter of 202 mm and a tire width of 54 mm. The motor-wheel is mounted on an aluminum fork supported by a commercial slewing-ring bearing, as shown in Fig. 15.

The slewing-ring bearing is attached to the main flange, which is fixed to the tubular frame of the wheelchair by four clamps. The bearing's rotating ring is connected on one side to the fork and on the other to a worm gear that engages with a worm driven by a commercial stepper motor NEMA 23, rated voltage of +24 VDC, holding torque 3.3 Nm, and 1.8° step angle, produced by LIN

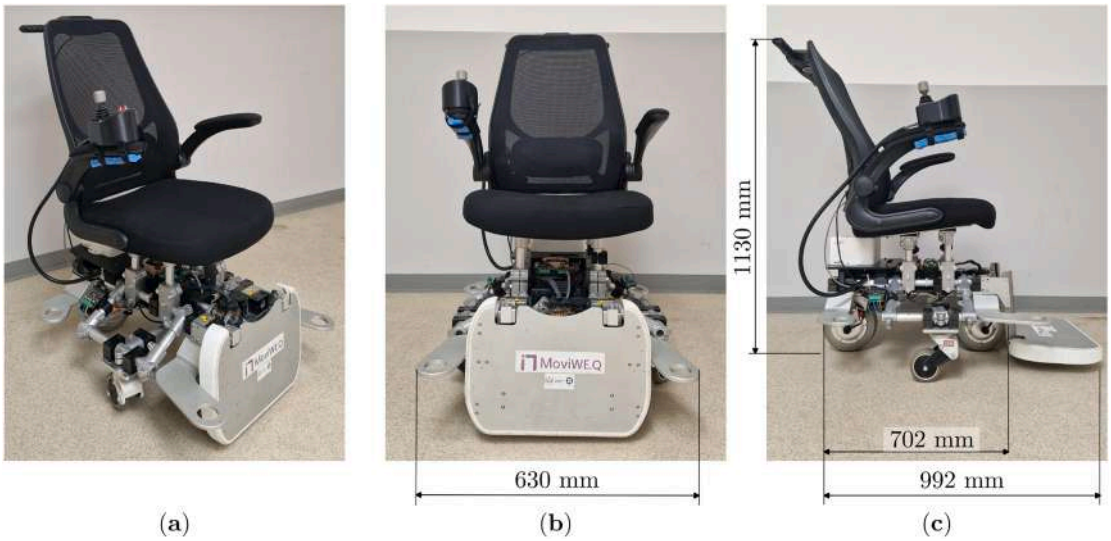

Fig. 14. MoviWE.Q prototype: (a) 3D view, (b) front view, (c) side view.

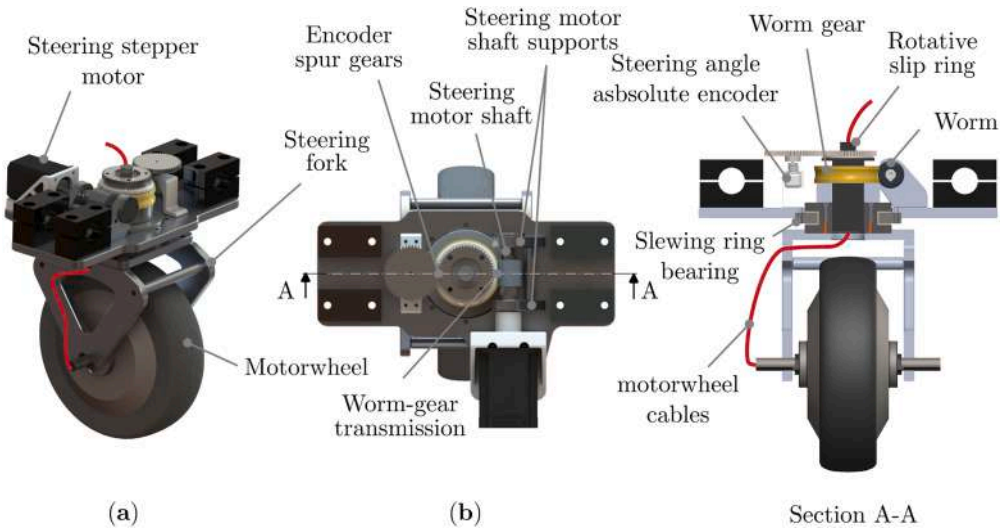

Fig. 15. Locomotion unit executive design: (a) 3D render view, (b) top view, (c) section $A - A$.

ENGINEERING. Dedicated supports are included for the worm-gear shaft to eliminate radial and axial loads on the motor supports. To ensure unrestricted steering rotation, an electrical slip ring is used to transmit power and control signals to the motor-wheel. Steering angle measurement is performed using an absolute optical encoder coupled through a spur-gear transmission.

The wheelchair MoviWE.Q has four contact points with the ground. Thus, a proper mechanical design of the wheel suspensions must be foreseen to guarantee steady floor contact and stability in every condition. It should be underlined that, because of the indoor application environment, the design requirements of the suspension system are not as stringent as they will be for an outdoor wheelchair, designed to move at high speed and deal with the presence of challenging architectural barriers. For this reason, the prototype of MoviWE.Q adopts a straightforward suspension system on the passive castor wheels that is sufficient to deal with four contact points and light ground unevenness. It should be noted that formal dynamic tipping/stability modeling and validation are beyond the scope of this article that focuses on the mobility improvements associated with the adoption of the swerve-drive locomotion system on an EPW. Nevertheless, formal stability quantification is essential for safety and commercial certification and it will be investigated in future works.

The chassis structure is constructed from aluminum tubes, T-shaped connectors, and aluminum plates. The tubes feature an outer diameter of 25 mm and a wall thickness of 2 mm, except for the primary longitudinal tubes, which have a wall thickness of 5 mm to ensure sufficient structural rigidity.

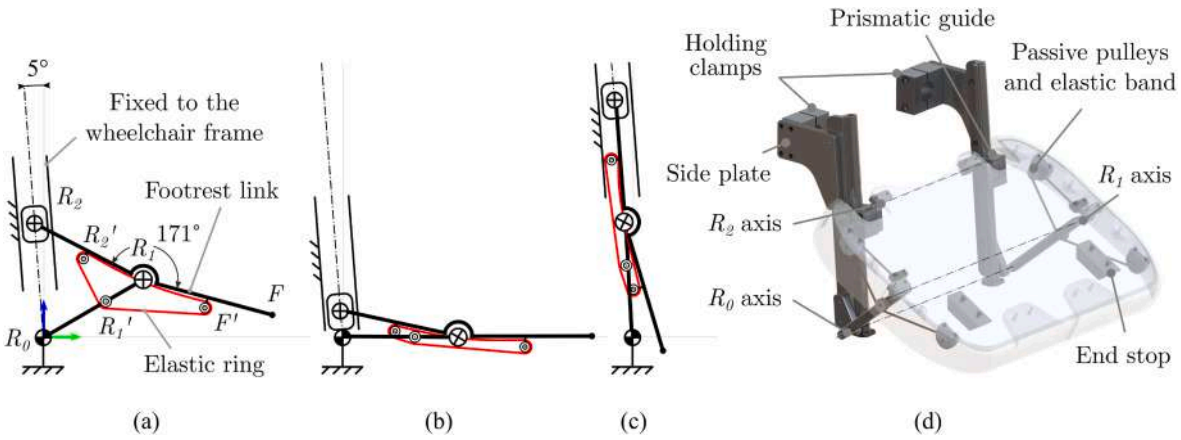

Fig. 16. Footrest functional scheme in different configurations: (a) generic configuration, (b) open configuration, (c) closed position. (d) Rendered view of the footrest mechanism executive design.

The footrest mechanism is designed to avoid interference with the feet during the opening/storage motion. To achieve this, the footrest platform is connected to the frame via a Scott-Russel mechanism as shown in Fig. 16. Moreover, the mechanism has a bi-stable behavior to lock the footrest in the open or closed configuration. The footrest mechanism can be defined entirely in the longitudinal plane (i.e., $x = 0$ plane of r.f. $\{b\}$), as shown in Fig. 16(a), (b), and (c). The footrest platform is connected, through the revolute joint R_2, to a carrier that slides on an inclined prismatic guide, and it is connected to a crank through the revolute joint R_1. The crank on the opposite end are connected to the frame through the revolute joint R_0. The bi-stable behavior is achieved by adopting an elastic band installed on the passive pulleys R_1', R_2', and F'.

A rendered view of the footrest mechanism is presented in Fig. 16(d). The prismatic guide fixed to the wheelchair chassis consists of two commercial cylindrical guides (IGUS, WS-16-UNGEBOHRT) and two matching carriages (IGUS, WJ200UM-01-16-AL). These cylindrical guides were cut to length and machined with additional mounting holes to secure them to the chassis via custom-designed lateral flanges and clamps, as well as to facilitate the installation of two mechanical end stops. The revolute joints are constructed using commercial hinge bases paired with 6 mm diameter cantilever shafts. The footrest plate itself is fabricated from a 5 mm thick aluminum plate, whereas the protective lateral covers are 3D-printed. Each tension band is composed of an inextensible section of thin rope connected in series with a linear traction spring. This configuration enables precise regulation of the elastic band's preload, while allowing the overall stiffness of the mechanism to be modified by replacing the spring component.

4.3. Electronic control unit

This section presents the electronic control unit of the wheelchair base platform, that has to fulfill the following tasks:

1. manage the power supply from the battery to the motor drivers and logic-level circuits;
2. read the input coming from the 3-axes joystick (manual mode) or sensorized handlebar (assisted mode) or the high-level onboard PC (autonomous mode);
3. computes the inverse velocity kinematics of the base-platform to evaluate the actuated variables references to exhibit the desired velocity twist, according to Algorithm 1;
4. read the current state of the platform from the encoders mounted on the steering shafts and from the hall sensors installed on the traction wheels;
5. effectively controls the actuated degrees of freedom: closed-loop controls to make the current state of the platform as close as possible to the actuated variables references.

A schematic representation of the low-level control system architecture is presented in Fig. 17. The low-level control module is designed around a USB-based microcontroller development unit, the Teensy 4.1 produced by PJRC, which is programmed in C++ using the Arduino IDE environment.

The traction wheel brushless motor drivers are commercial ODrive Pro-units manufactured by ODrive Robotics. These drivers communicate with the microcontroller via CAN-bus, operate within an input DC voltage range of $[15, 58]$ V, and support a maximum continuous motor current of 20 A in free air.

The steering stepper motor drivers are commercial DM556T units from STEPPERONLINE, which operate within an input DC voltage range of $[20, 50]$ V and support a maximum current of 6 A in free air. These stepper drivers are commanded by the microcontroller via three digital signals: step, direction, and enable.

To measure the steering angles, the system utilizes commercial EMS22A30 non-contacting absolute encoders from Bourns. These sensors communicate with the microcontroller via a Serial Peripheral Interface (SPI), operate at an input voltage of 3.3 V, and provide an angular resolution of 0.35°.

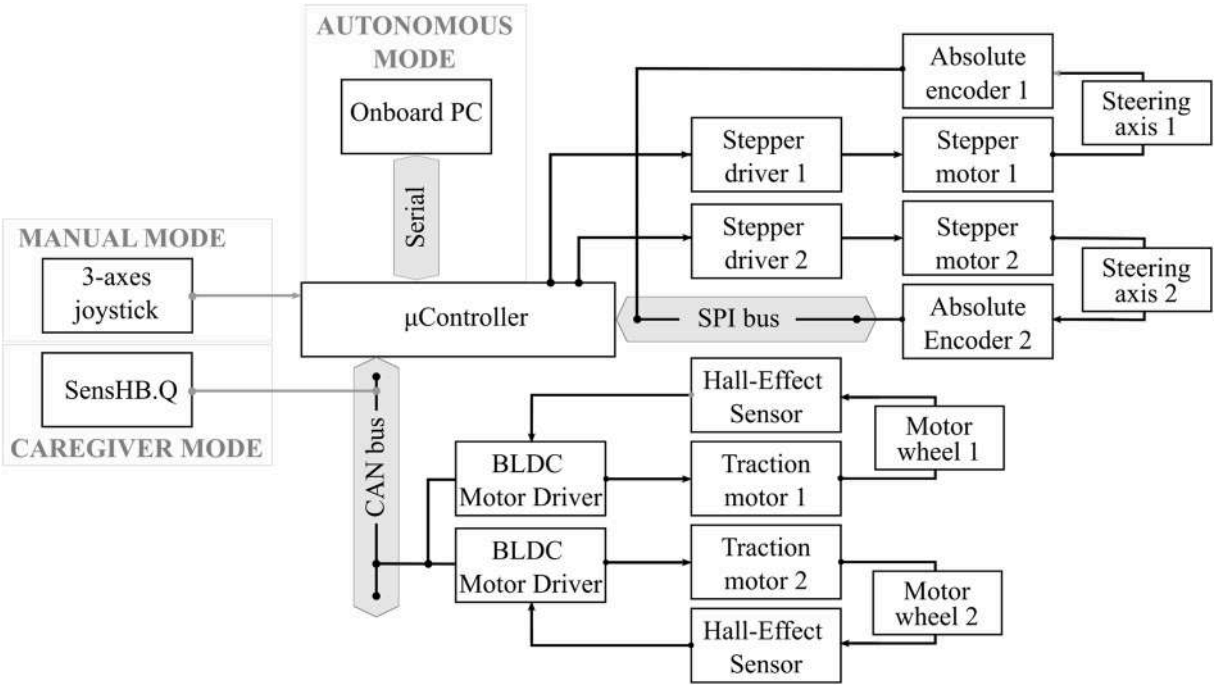

Fig. 17. Schematic representation of the electronic control unit of the wheelchair base.

The power management unit is composed of a relay that is activated by two switches in a series: an ON/OFF switch (normally closed) and an emergency button (normally opened). The motor drivers are powered when both switches are activated. If the emergency button is `OFF` and the ON/OFF switch is `ON`, the motor drivers are deactivated, while the low-level logic remains powered. This feature simplifies the debugging/testing phase while ensuring a certain level of safety. Moreover, two voltage regulators are installed on the electronic control unit board: the R-78C5.0–1.0 and the R-78C3.3-1.0 by RECOM Power. These voltage regulators generate two power supply lines at 5.0 V and 3.3 V for the microcontroller and the other sensors. Finally, the electrical power system is supplied by a $7S$ lithium-ion polymer (LiPo) battery pack, providing a nominal capacity of 30 Ah. The autonomy of the overall system in an indoor setting with flat ground and a user of about 80 kg was estimated experimentally. The result is an autonomy of about 3 to 4 hours of continuous driving with standard acceleration and deceleration maneuvers (like those performed to move from one point to another between different rooms of an apartment).

5. Force-sensitive interface for caregivers

As presented in the Introduction (Sections 1.3 and 1.4), research concerning drive interfaces specifically designed for caregivers remains limited. In particular, significant advancements can be made in developing cost-effective, force-sensitive interfaces tailored for omnidirectional or pseudo-omnidirectional EPWs. To address this gap, the authors [74] presented the first prototype of the force-torque-sensitive handlebar, SensHB.Q. The technology is covered by an Italian patent titled *Sensorized Handlebar for Motorized System* (Priority Date: 27/02/2024, Priority Number: 102024000004177). This section summarizes the development of the newest version of SensHB.Q, presenting its conceptual framework (Section 5.1), functional design (Section 5.2), electronic control unit configuration (Section 5.4), and physical prototype implementation (Section 5.3).

5.1. Concept

As a drive interface for omnidirectional or pseudo-omnidirectional mobile systems, SensHB.Q must satisfy several key requirements:

- *drivability*: The interface must enable drivers to exert complete and precise control over the motorized device;
- *ergonomics*: The handle should be designed for comfort, minimizing physical strain, incorrect posture, or discomfort during extended operation;
- *ease of use*: Ideally, the interface must be intuitive and straightforward to operate, requiring little to no specific training for the operator;
- *safety*: The system must robustly distinguish between intentional driver commands and accidental inputs, ensuring the safe operation of the motorized device at all times.

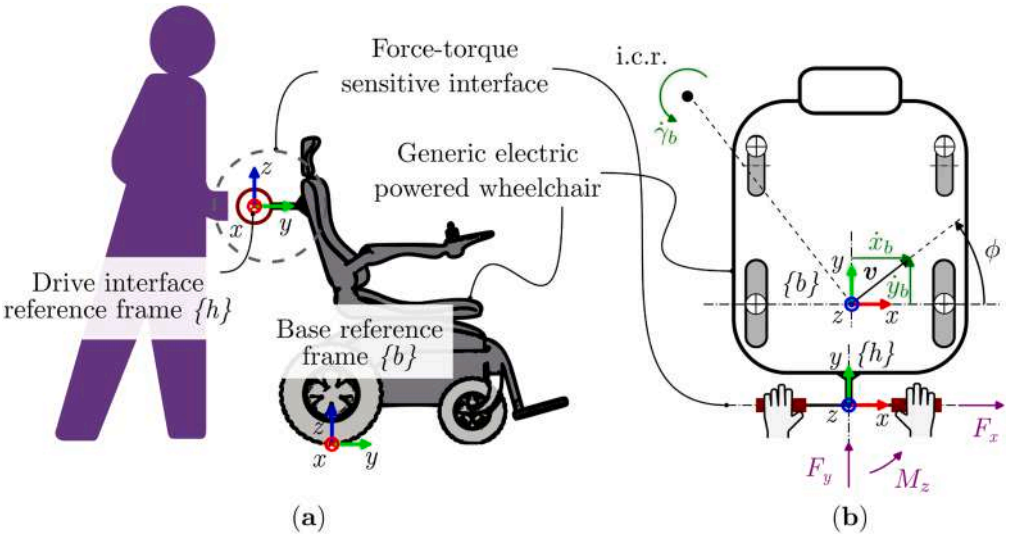

Fig. 18. Concept representation of the drive interface, inputs, and reference frames definition: (a) side view, (b) top view.

To meet these operational criteria, SensHB.Q measures three distinct components of the caregiver's applied wrench. These force/torque inputs are subsequently mapped into velocity commands for the EPW, as illustrated in Fig. 18. By utilizing direct force/torque inputs, the system achieves a highly intuitive user experience, as it directly mirrors the natural physics of manual manipulation, where human operators apply forces and torques aligned with their intended direction of motion. At least, three components of the applied wrench must be measured to drive omnidirectional or pseudo-omnidirectional motorized systems, thus the interface must be properly sensorized.

Commercial multi-axis force-torque sensors are prohibitively expensive, typically ranging from €5000 to €12000 depending on the brand (e.g., Bota Systems, Kistler, and Futek). Consequently, they are poorly suited for a drive interface where cost-effectiveness is a critical factor for the technology's adoption and success. To address this constraint, SensHB.Q is designed around a planar 3-DOF (degrees of freedom) mechanism that is isostatically constrained by three uniaxial load cells. These components are significantly more economical than multi-axis alternative sensors; as a reference, the three uniaxial load cells utilized in this project cost approximately 150€ each.

Finally, it is crucial to ensure that accidental impacts with force-sensitive interfaces do not trigger unintentional motions of the motorized system. To robustly distinguish between intentional driver commands and accidental inputs, proximity, or touch sensors are integrated directly into the ergonomic handles of the interface. This setup determines whether the driver is properly grasping the device. The interface remains active, and velocity commands are transmitted to the wheelchair control system, only when a valid grip state is verified.

5.2. Functional design

The primary characteristic of SensHB.Q is its capability to resolve three independent components of the applied wrench using only three uniaxial load cells. To achieve this, the SensHB.Q architecture utilizes a six-bar linkage mechanism, as schematically illustrated in Fig. 19. Link 0 represents the ground link, which is rigidly fixed to the backrest of the wheelchair. Link 3 (red link in Fig. 19) serves as the coupler link that connects the two ergonomic grips, which are embedded with capacitive switches to detect the presence of the driver. This coupler link (Link 3) is kinematically constrained relative to the ground link (Link 0) via two symmetric $2R$ serial chains, denoted by the joint sequences $A_0 - A - B$ and $C - D - D_0$. Finally, three uniaxial load cells (LC1, LC2, and LC3) are positioned to isostatically constrain this 3-DOF six-bar linkage.

This constitutes the final iteration of the interface's design process. For further technical details regarding the alternative architectures and preliminary configurations that were considered, the interested reader is referred to the authors' previous study [74].

The caregiver applies the forces $F_{x,user}$ and $F_{y,user}$ and the torque $M_{z,user}$ and the system measures the three load cells reactions F_{lcj}, where $j = 1, 2, 3$ (F_{lcj} is the force along the load cell axis applied at the end points and positive when the load cell is under tension). All the other components of the applied wrench are supported by the six-bar linkage. Given the free-body diagram and the geometrical parameters l_1 and l_2 illustrated in Fig. 19(b), the equilibrium of forces and torques of the handlebar (l_{k3}), the relation between the forces measured by the uniaxial load cells F_{lcj} ($j = 1, 2, 3$), defined positive under traction, and the components of the

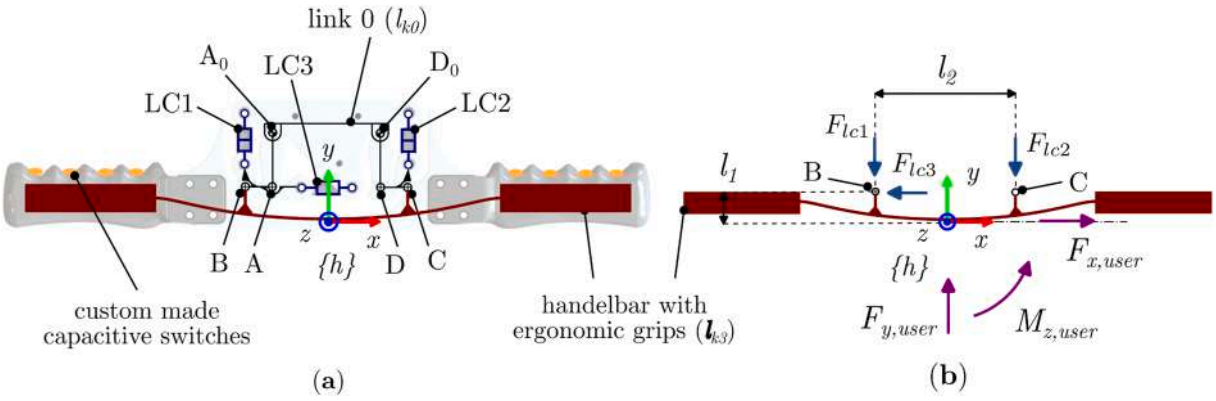

Fig. 19. SensHB.Q functional design: (a) functional scheme on top of a top view render of the prototype in transparency, (b) free-body diagram (notice that under this load state all load cells are under compression, therefore each F_{lci} is negative).

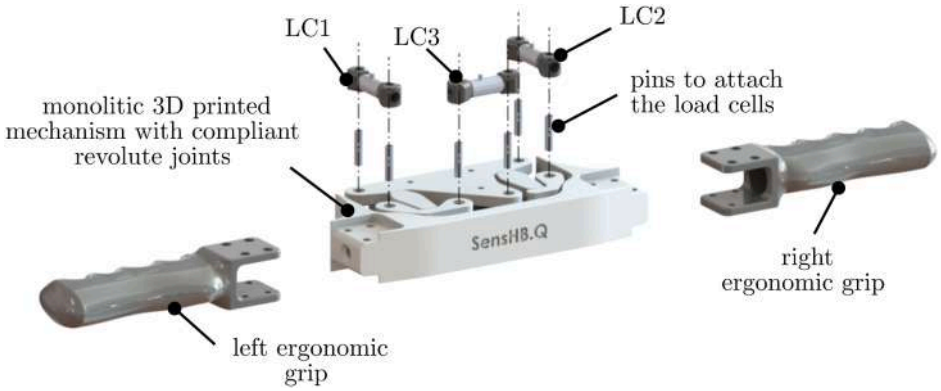

Fig. 20. Render exploded view of SensHB.Q.

user wrench is described by Eq. (21).

$$ {}^{h}\begin{bmatrix} M_z \\ F_x \\ F_y \end{bmatrix}_{user} = -\begin{bmatrix} \frac{l_2}{2}(F_{lc1} - F_{lc2}) - l_1 F_{lc3} \\ F_{lc3} \\ F_{lc1} + F_{lc2} \end{bmatrix} = -\begin{bmatrix} \frac{l_2}{2} & -\frac{l_2}{2} & -l_1 \\ 0 & 0 & 1 \\ 1 & 1 & 0 \end{bmatrix} \begin{bmatrix} F_{lc1} \\ F_{lc2} \\ F_{lc3} \end{bmatrix} \tag{21} $$

5.3. Prototype

This section presents the newest version of the force-sensitive interface SensHB.Q. With respect to the previous version described in detail in [74], the main improvement in the newest version is the adoption of a 3D-printed monolithic mechanism with built-in flexure hinges instead of conventional revolute joints and separated links. Compliant revolute joints are particularly suited for this type of application. The main advantage is the elimination of static friction in revolute joints that can alter the force measurements. Moreover, fatigue issues related to flexure hinges are negligible in this application because the system is an isostatic structure and, ideally, no range of motion is required from the flexure hinges. This improved version has significantly reduced the part count: the original version consisted of twelve 3D printed components and two aluminum profiles, whereas the new version comprises only three 3D printed parts (excluding screws and nuts). This simplification improves both manufacturing and assembly. Fig. 20 shows a render exploded view of the main structure of SensHB.Q.

Fig. 21(a) and (b) depict the SensHB.Q prototype, and in Fig. 21(c) the interface is mounted on the pseudo-omnidirectional EPW MoviWE.Q. The adopted load cells, model FLAE-100N, are produced and calibrated by Forsentek Co. The measurable load range is ±100N, the rated output is 0.2 mV/V, excitation at +5 V. Custom-made capacitive switches are installed in the ergonomic grips beneath the driver's fingers, as shown in Fig. 21(b). These sensors function as dead-man switches, enabling or disabling the force-torque measurements. In this way, accidental impacts on the device do not generate unintended commands for the motorized system.

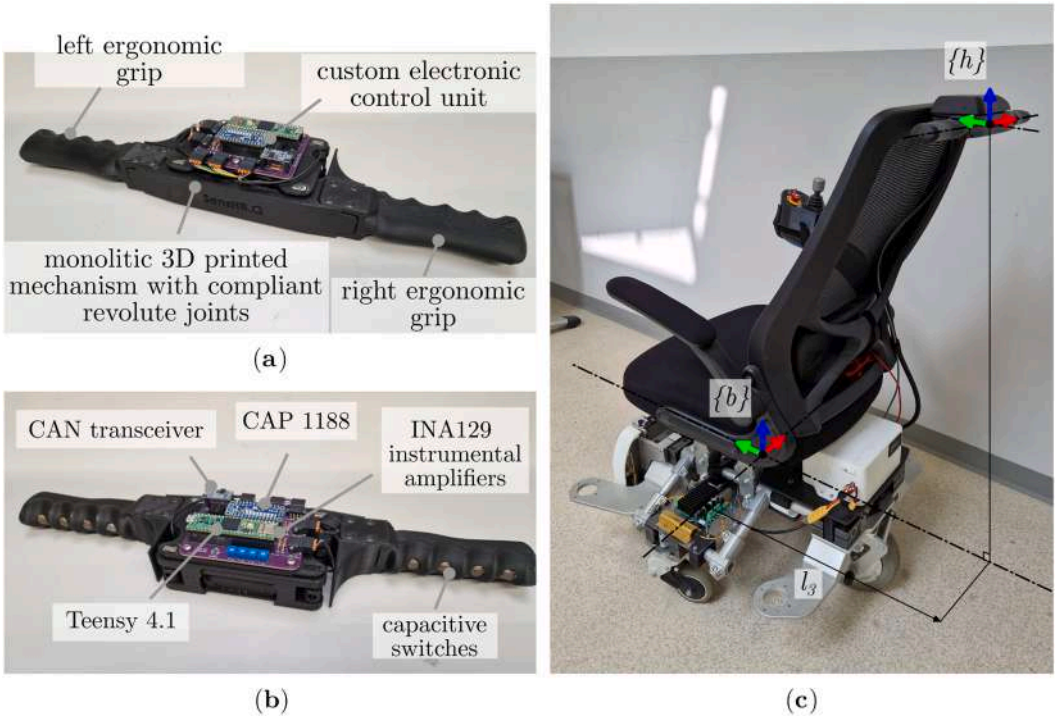

Fig. 21. SensHB.Q prototype: (a) front view, (b) back view, (c) SensHB.Q mounted on MoviWE.Q.

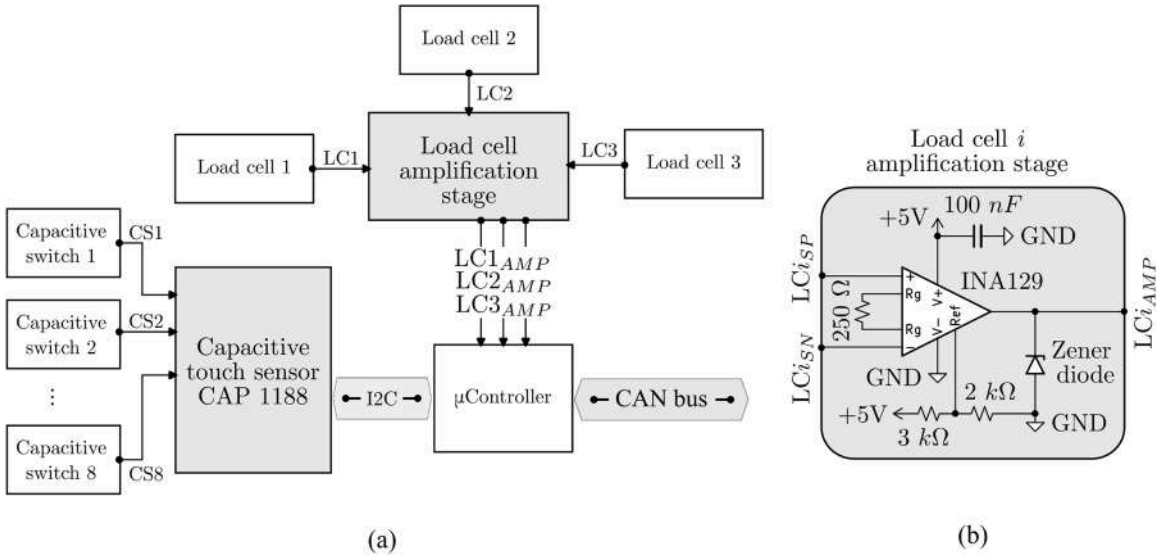

Fig. 22. (a) schematic representation of the control unit of the force-sensitive interface SensHB.Q; (b) load cell i amplification stage electronic scheme.

5.4. Electronic control unit

This section describes the electronic control unit (ECU) of the force-sensitive interface SensHB.Q. The ECU, shown in Fig. 22(a), is designed around a microcontroller, a Teensy 4.1 produced by PJRC, that reads the amplified load cell signals and the status of the capacitive switches. The raw voltage difference of the load cell j (i.e., $\Delta V_{LC_j} = LCj_{SP} - LCj_{SN}$) is amplified using a commercial instrumental amplifier, the INA129 by Texas Instrument. The amplification gain is designed to convert the raw voltage difference $\Delta V_{LC_j} \in [-5, +5]$ mV into an amplified load cell voltage difference $\Delta V_{LC_j,AMP} \in [+1, +3]$ V. The electronic circuit used for the amplification of the load cell is illustrated in Fig. 22(b).

After the amplified load cell signals are read, the signals are converted into actual forces considering the total gain of 0.050V/N, and a linear static characteristic (i.e., load cell nonlinearity ±0.3% of the rated output). Eq. (21) is used to compute the applied wrench components with respect to $\{h\}$, and then the wrench components are transposed into the base reference frame $\{b\}$ (defined in Fig. 21(c)) using Eq. (22).

$$ {}^{b}W_{user} = {}^{b}\begin{bmatrix} M_z \\ F_x \\ F_y \end{bmatrix}_{user} = \begin{bmatrix} 1 & l_3 & 0 \\ 0 & 1 & 0 \\ 0 & 0 & 1 \end{bmatrix} {}^{h}\begin{bmatrix} M_z \\ F_x \\ F_y \end{bmatrix}_{user} \tag{22} $$

To compute the reference velocity twist for the pseudo-omnidirectional EPW, the wrench components are used as inputs to a simplified dynamic model. This choice to use a simplified dynamic model instead of a validated physical model of the complete wheelchair and occupant originates from the idea to develop an interface that (ideally) could be used, as it is, on other omnidirectional or pseudo-omnidirectional motorized systems such as mobile robots of heavy-duty motorized trolleys.

A simple contact model based on Coulomb's dry friction model is used to obtain an intuitive dynamic response of the system. The entire system is modeled as a box on a plane with dry friction. The static and kinetic friction coefficients are μ_s and μ_k. The gravity force is acting in the negative z-direction, thus the vertical reaction force is $\mathbf{N} = mg\hat{\mathbf{z}}$. The friction force acting on the system is $\mathbf{F}_f = F_f\hat{\mathbf{F}}_f$, where $\hat{\mathbf{F}}_f = -\hat{\mathbf{v}}$. The limiting friction force is defined as $\mathbf{F}_{f,max} = \mu_s mg\hat{\mathbf{F}}_f$. If the body is still, the friction force is $F_f = \mu_s mg$, if $\sqrt{F_{x,user}^2 + F_{y,user}^2} \leq \mu_s mg$, and $F_f = \mu_k mg$, if $\sqrt{F_{x,user}^2 + F_{y,user}^2} > \mu_s mg$. If the body is moving, the friction force is equal to $\mathbf{F}_f = F_f\hat{\mathbf{F}}_f = -\mu_k mg\hat{\mathbf{v}}$.

Regarding the yaw rotation, let's consider a contact area between the ground and the box as a thin ring of radius r_f. Then, the limiting friction torque is $M_{f,max} = \mu_s mg\, r_f$. When the system is not moving the friction torque is opposite the applied friction force, while when the system is rotating the friction torque is opposite to the yaw rotation. If the body is still, the friction torque is $M_f = \mu_s mgr_f$, if $|M_{z,user} + l_3F_{x,user}| \leq \mu_s mgr_f$, and $M_f = \mu_k mgr_f$, if $|M_{z,user} + l_3F_{x,user}| > \mu_s mgr_f$. If the body is rotating, the friction torque is equal to $\mathbf{M}_f = M_f\hat{\mathbf{M}}_f = -\mu_k mgr_f\hat{\omega}$.

Given these premises, the equilibrium of the box on the plane can be written as:

$$ \begin{cases} I_z\ddot{\gamma}_b - \mathbf{M}_f^T\hat{z} = M_{z,user} + l_3F_{x,user} \\ m\ddot{x}_b - \mathbf{F}_f^T\hat{x} = F_{x,user} \\ m\ddot{y}_y - \mathbf{F}_f^T\hat{y} = F_{y,user} \end{cases} \quad \leftrightarrow \quad M\dot{\mathbf{V}}_b + f(\mathbf{V}_b) = \Gamma W_{user} \tag{23} $$

where M is the mass matrix, $f(\mathbf{x})$ collects the friction contributions, ΓW_{user} the driver input wrench contribute.

$$ M = \begin{bmatrix} I_z & 0 & 0 \\ 0 & m & 0 \\ 0 & 0 & m \end{bmatrix}; \qquad \Gamma = \begin{bmatrix} 1 & l_3 & 0 \\ 0 & 1 & 0 \\ 0 & 0 & 1 \end{bmatrix}; \tag{24} $$

Solving eq. (23) in the discrete time domain, the estimator equation can be written as in (25).

$$ \mathbf{V}_b(k+1) = \mathbf{V}_b(k) + M^{-1}(\Gamma W_{user} - f(\mathbf{V}_b))dt \tag{25} $$

In Eq. (25), the current status $\mathbf{V}_b(k)$ of the system is needed to compute the new state estimation. If the feedback $\mathbf{V}_{b,fb} = \begin{bmatrix}\dot{\gamma}_b & \dot{x}_b & \dot{y}_b\end{bmatrix}_{fb}^T$ of the system is available and accurate, it should be used as $\mathbf{V}_b(k)$. Odometry based velocity twist feedback can be computed using (10), from the feedback steering angles $\delta_{1,fb}$, and $\delta_{2,fb}$, and the wheel angular velocity feedback $\dot{\theta}_1$, and $\dot{\theta}_2$. During the experimental campaign detailed in Section 6.3 the odometry based velocity feedback has been used.

The adoption of a simplified dynamic model in the reference velocity twist evaluation provides several physical parameters that can be tuned to modify the driving experience. The parameters have been tuned manually using an iterative procedure based on the driving preferences of the calibration team composed by a subset of the authors of this work. In general, lowering m reduces the perceived weight of the system. The parameter $r_{I_z,m}$ determines the balance between the effort required for rotation versus translation. Finally, μ_s, μ_k, and r_f adjust the perception of friction. After the tuning phase, the following numeric values have been selected: $m = 5$ kg, $r_{I_z,m} = I_z/m = 0.03$ m^2, $r_f = 0.2$ m, $\mu_s = 0.08$, and $\mu_k = 0.079$. These numerical values have been kept constant for the experimental campaign presented in Section 6.3.

6. Experimental validation

6.1. Wheelchair performance evaluation and ISO tests for indoor mobility

To evaluate the effectiveness of MoviWE.Q, a series of tests were conducted in indoor environments. First, tests to measure wheelchair dimensions, mass, and maneuvering space, as outlined in ISO 7176-5, were performed. In particular, the following important wheelchair characteristics have been evaluated:

- *total mass*;
- *overall width*;
- *overall height*;

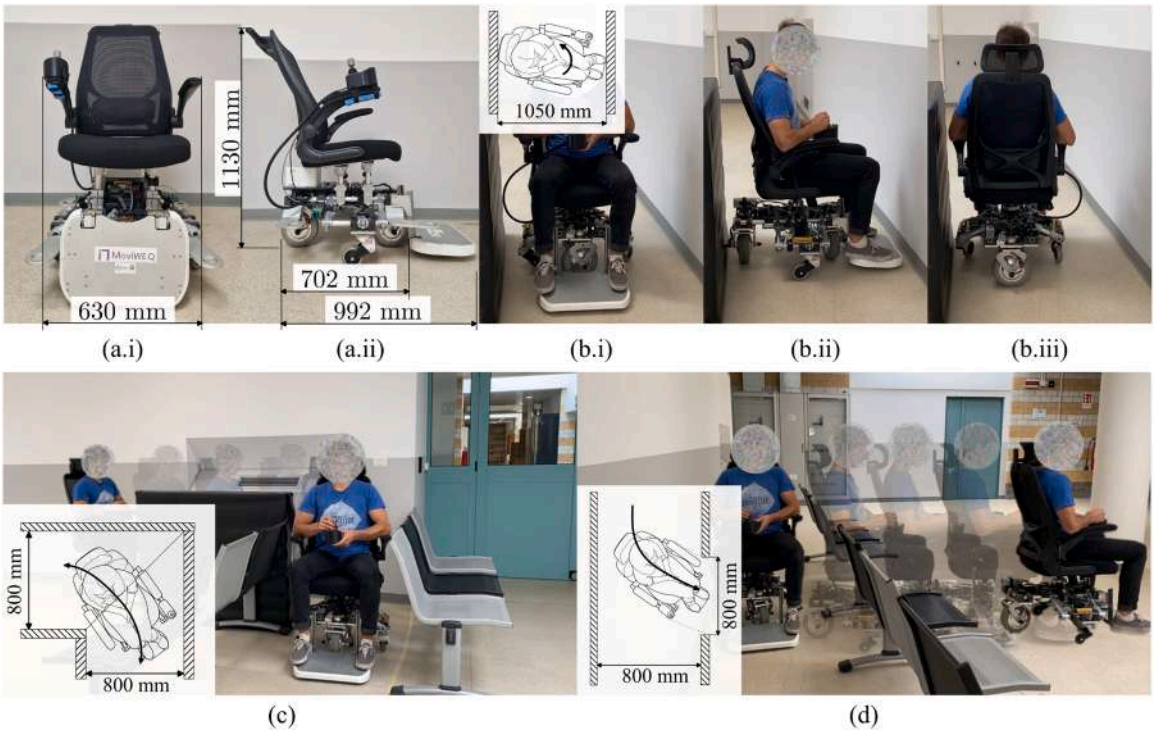

Fig. 23. MoviWE.Q test according to ISO 7176-5: (a) relevant dimensions; (b) pivot width test; (c) required width of angled corridor; (d) required corridor width for side opening.

Table 1
MoviWE.Q dimensions, mass, and maneuvering space as determined in ISO 7176-5. The ISO recommended maximum values originate from ISO/TR 13570-2:2014 which complements ISO 7176-5.

Description	Value	ISO recommended maximum value
Total mass	41 kg	100 kg
Overall width	630 mm	700 mm
Overall height	1130 mm	1200 mm
Full overall length	992 mm	1200 mm
Reduced overall length	702 mm	1000 mm
Pivot width	1050 mm	1400 mm
Required width of angled corridor	800 mm	990 mm
Required corridor width for side opening	800 mm	1290 mm

- *full overall length*: the total length of the wheelchair with footrest opened without occupant;
- *reduced overall length*: the total length of the wheelchair without footrest and occupant;
- *pivot width*: minimum distance between two vertical and parallel walls between which a wheelchair can turn through 180° with one single and continuous turning maneuver (Fig. 23(b));
- *required width of angled corridor*: minimum width of a corridor with a right-angled turn in which the wheelchair can be driven in both forward and rearward directions(Fig. 23(c));
- *required corridor width for side opening*: minimum width of a corridor necessary to permit the wheelchair to move forwards in or out of the corridor through an open doorway of defined width in one wall (Fig. 23(d)).

The numerical results are presented in Table 1 together with the recommended maximum values from ISO 7176-5.

The tests conducted in accordance with ISO 7176-5 reveal that MoviWE.Q has a compact footprint and exhibits high mobility in narrow spaces. However, these tests are designed primarily for conventional differential-drive EPWs and are inadequate for assessing the pseudo-omnidirectional capabilities of MoviWE.Q.

To qualitatively test the system's effectiveness at navigating in narrow spaces full of obstacles, the test tracks schematically represented in Fig. 24(a) and (b) are used. These tracks are meant to simulate everyday situations, such as navigating within a classroom. In the first test, the wheelchair is required to approach a school desk using purely translational motion. In the second test, the pseudo-omnidirectional mobility of the wheelchair is leveraged to move away from the desk while simultaneously rotating 180°

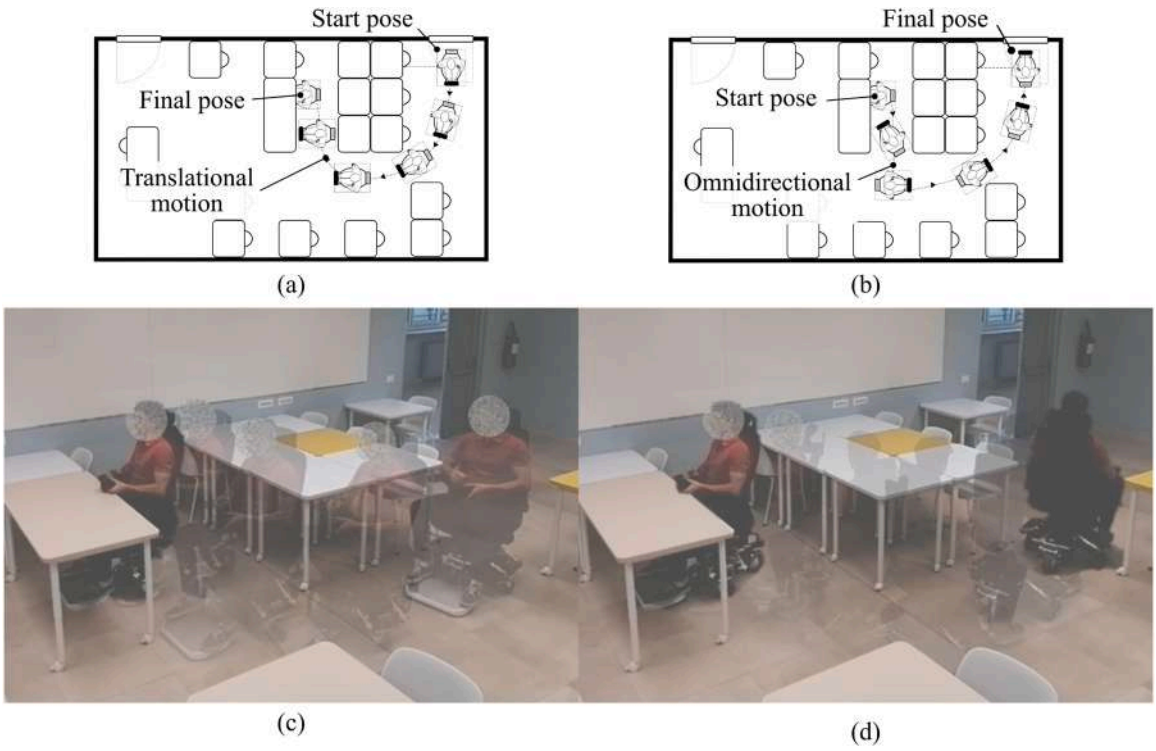

Fig. 24. MoviWE.Q manual mode mobility test: (a) environment scheme and motion definition for test 1; (b) environment scheme and motion definition for test 2; (c) test 1 motion execution; (d) test 2 motion execution.

Table 2
Root-mean-square errors of the wrench components F_x, F_z and M_y wrt $\{LC_{6A}\}$ between the force/torque measurements of SensHB.Q and the commercial six-axis force sensor.

Test N°	RMS_{F_x} (N)	RMS_{F_z} (N)	RMS_{M_y} (Nm)	Test N°	RMS_{F_x} (N)	RMS_{F_z} (N)	RMS_{M_y} (Nm)
1	2.10	1.78	0.17	6	1.97	1.97	0.17
2	1.79	1.51	0.17	7	1.84	2.25	0.16
3	2.28	1.58	0.19	8	1.74	2.31	0.15
4	2.22	2.03	0.19	9	1.48	2.03	0.13
5	2.10	1.78	0.15	10	2.00	1.98	0.16

to exit the room. Throughout the tests, the wheelchair must also maneuver through a passage that is 700 mm wide. The execution of these tests is depicted in Fig. 24(c) and (d) through a series of multi-exposed images. Each test was performed five times, achieving a success rate of 100%.

During the experimental tests, the pseudo-omnidirectional mobility of the wheelchair demonstrated its effectiveness in navigating challenging environments and completing tasks that are not feasible with a conventional EPW. Additionally, this pseudo-omnidirectional capability proved advantageous from a control perspective. Specifically, when making turns to pass through narrow passages, the ability to decouple the velocity vector direction from the wheelchair's orientation allows the user to correct their trajectory by making small lateral adjustments.

6.2. Force-sensitive interface validation tests

This section presents the bench tests conducted to measure the effectiveness of the newest version of SensHB.Q in measuring the components applied by the user. To do so, the force-sensitive interface was mounted on a commercial six-axis force-torque sensor, the SensOne by BOTA SYSTEMS, as illustrated in Fig. 25. During the tests, the user was instructed to apply random wrenches to the force-sensitive interface, and the wrench components were acquired simultaneously from SensHB.Q and the commercial sensor. To compare the measurements of the two systems, the reading of the sensorized handlebar are transposed in the reference frame $\{LC_{6A}\}$.

To quantitatively compare the two measurements, the root-mean-square errors of the wrench components F_x, F_z and M_y wrt $\{LC_{6A}\}$ are reported in Table 2. As an example, the measurements of test number 2 are shown in Fig. 26.

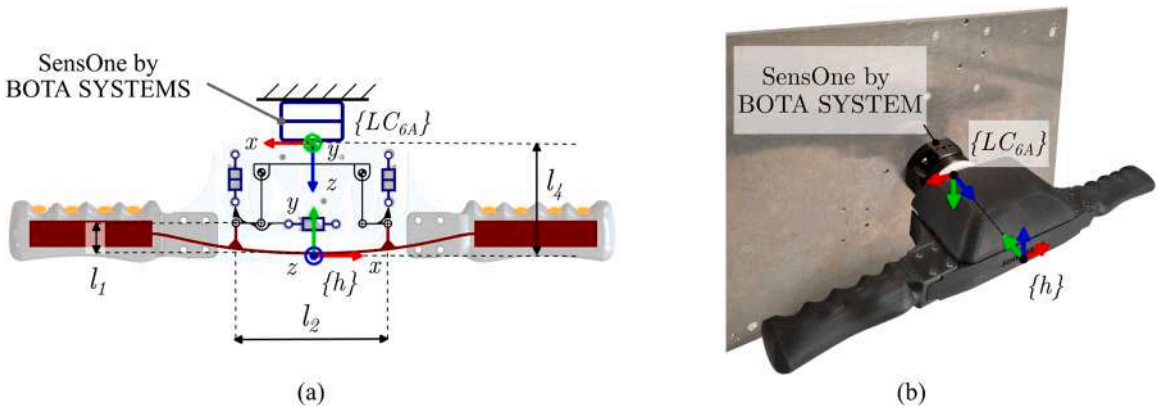

Fig. 25. SensHB.Q experimental validation setup: (a) schematic representation and parameters definition; (b) photo of the experimental setup.

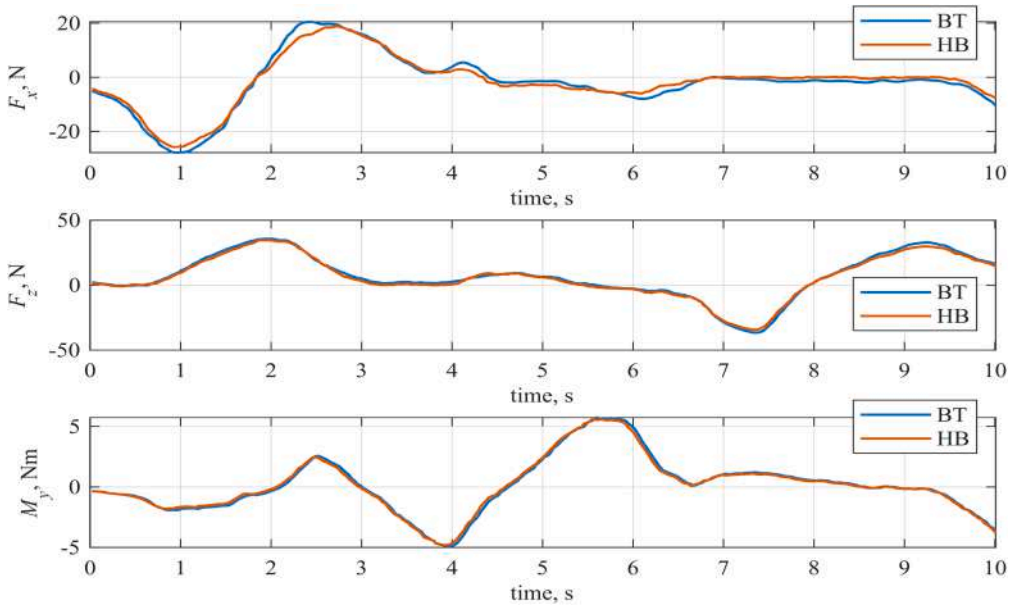

Fig. 26. Acquired wrench components in the $\{LC_{6A}\}$ reference frame during test number 2. Notice that the acronym "HB" stands for the wrench components measured with SensHB.Q, while "BT" for the commercial six-axis force torque sensor by BOTA SYSTEMS.

When evaluating these results, it is essential to consider the intended application of the sensorized handlebar, specifically its purpose of gathering the intention of caregiver regarding the desired motion of the wheelchair. From this perspective, the measurements appear promising for testing the functionality of the SensHB.Q on the pseudo-omnidirectional wheelchair MoviWE.Q given the small root-mean-square (RMS) errors: 1.95 N for F_x, 1.92 N for F_z, and 0.16 Nm for M_y (standard deviation: 0.24 N for F_x, 0.26 N for F_z, and 0.02 Nm for M_y).

6.3. *Wheelchair experimental drive test using the force-sensitive interface*

Experimental tests were carried out on the developed prototypes to validate the performance of MoviWE.Q and the force-sensitive interface SensHB.Q. The experimental campaign involved 18 volunteers. The participant population ranged in age from 25 to 64 years (mean age: 31 years). This experimental campaign focuses on the *Assisted drive* mode for caregivers. For this reason, the following eligibility criteria were adopted: working age, no mobility limitation, and no previous experience with the system. After a ten minute driving session needed to get used to MoviWE.Q and its drive-interface SensHB.Q, each participant was instructed to drive the system using the force-sensitive interface along a predefined track inside the university laboratory.

It should be clarified that this population does not include professional caregivers and that no real-case applications have been studied. Thus, the results should be intended as an initial assessment under the laboratory conditions tested. Nevertheless, these experimental tests are essential to guide the future development of real-case application experimental campaign with professional

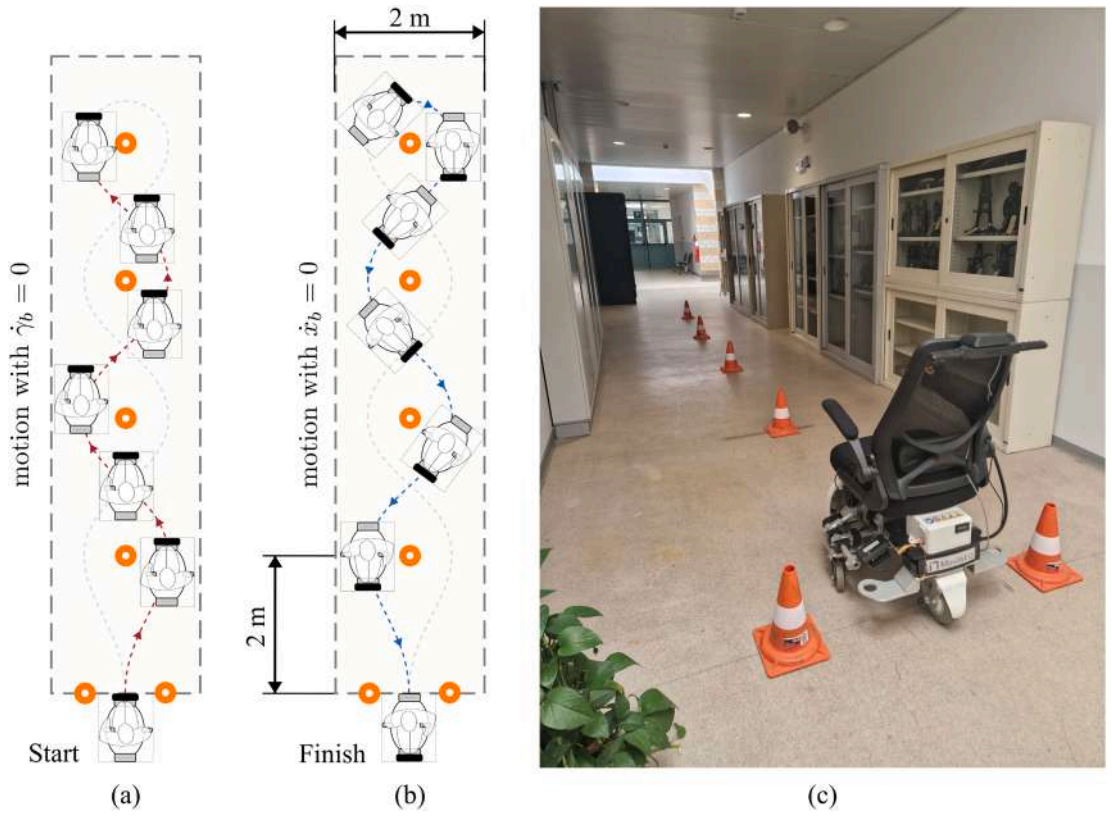

Fig. 27. Experimental setup: (a) scheme of the first part of the motion with $\dot{\gamma}_b = 0$ (pure translation movement), (b) scheme of the second part of the motion with $\dot{x}_b = 0$ (2D roto-translational motion), (c) photo of the experimental setup.

caregivers and family caregivers. Moreover, this experimental setup, given its simplicity, could be used by other researchers to assess the usability and workload of other EPW interfaces.

The experimental setup required driving the MoviWE.Q wheelchair along a track set up in the laboratory, as illustrated in Fig. 27. The track was defined within a 2-meter-wide, 10-meter-long corridor with traffic cones placed along the centerline at 2-meter intervals. Participants navigated the wheelchair in a slalom pattern back and forth along the track. During the first phase of the test, participants were instructed to maintain a constant heading (pure translational motion with $\dot{\gamma}_b = 0$). In the second phase, participants were asked to avoid lateral movements (2D roto-translational motion with $\dot{x}_b = 0$). Following the trial, a questionnaire collected participant ratings regarding system usability and perceived task workload. Usability and perceived workload were quantified using the System Usability Scale (SUS) and the NASA Task Load Index (NASA-TLX), respectively. During the tests, no user was seated on the wheelchair, but a weight of 50 kg was placed on the seat. Moreover, during the tests, the maximum absolute value of the linear velocity and the maximum absolute value of the yaw angular velocity were set respectively to 0.5 m/s and $\pi/4$ rad/s.

The SUS, introduced by John Brooke in 1996 [78], is a widely adopted instrument for assessing subjective usability, yielding a global score ranging from 0 to 100. It consists of a 10-item Likert scale with forced-choice responses, where participants rate their level of agreement on a five-point scale from *strongly agree* to *strongly disagree*. Positively framed statements occupy odd-numbered items, whereas negatively framed statements occupy even-numbered items. The SUS has been extensively applied in intelligent wheelchair evaluation. For instance, Callejas-Cuervo et al. [79] used it to evaluate a head-movement control interface (10 participants, mean SUS score of 78); Panchea et al. [80] evaluated a graphical user interface for smart powered wheelchairs (11 participants, mean SUS score of 68); and Zhang et al. [81] tested a gaze-tracking control interface (14 participants, mean SUS score of 78.21).

Subjective workload assessments were gathered using the NASA-TLX framework developed by the Human Performance Group at NASA Ames Research Center [82,83]. The NASA-TLX measures perceived workload across six descriptors: mental demand, physical demand, temporal demand, performance, effort, and frustration. Each dimension is evaluated on a 20-point subscale. The overall *TLX score* is derived by averaging these subscale ratings and rescaling the result to a range of 0 to 100, representing the overall perceived effort required for the task. Standard literature conventions categorize the final score into five workload levels: very low effort (0–9), low effort (10–29), moderate effort (30–49), high effort (50–79), and very high effort (80–100).

The results of the experimental campaign are summarized in Fig. 28. All participants successfully completed the slalom track using the SensHB.Q force-sensitive interface without collisions, achieving a 100% task completion rate. The aggregate mean SUS score was 83.1 ± 11.2 (mean value $\pm$ standard deviation), a median of 85, with an interquartile range (IQR) of 15 (the 95% Confidence Intervals

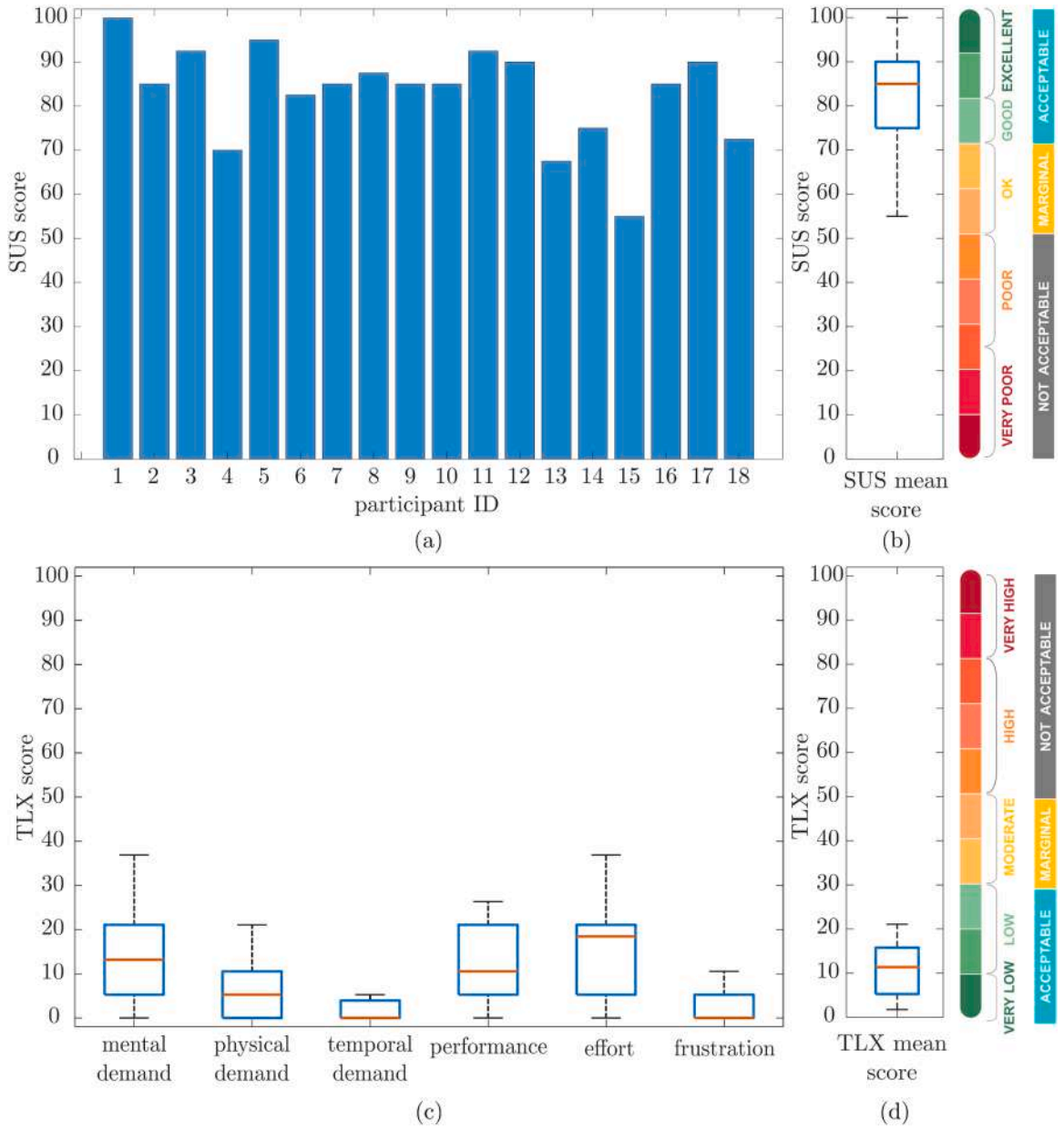

Fig. 28. Experimental test results: (a) SUS mean score for each participant, (b) box plot showing the aggregated data for the total SUS mean score, (c) box plots relative to the NASA - TLX indices for the six descriptors, and (d) box plot showing the aggregated data for the total TLX mean score.

(95% CI) computed using Student's t-distribution is [77.5, 88.6]) . Benchmark comparisons with alternative control interfaces, such as those previously cited, suggesting good-to-excellent usability, which is a promising result regarding the effectiveness of the proposed system. As shown in Fig. 28(b), the interquartile ranges of the aggregated SUS scores fall within the *Acceptable* range (encompassing good and excellent thresholds). It should be noted that Participant 15 rated the system around 55 points, corresponding to an *Ok* level of usability. While individual qualitative feedback detailing this lower score could not be retrieved, such variance is expected when testing early-stage physical and interface prototypes and it is the reflection of individual end-user variability.

The overall mean NASA-TLX score was 10.9 ± 6.2, placing the perceived workload near the boundary between the very-low and low effort categories (Fig. 28(d)). The median of the distribution was 11.4, with an IQR of 10.5 (95% CI computed using Student's t-distribution is [7.8, 13.9]). This is a promising result given that wheelchair manipulation can be physically demanding for caregivers. Specifically, the mean rating for the *physical demand* subscale was 8.5 on the rescaled 100-point TLX scale. Conversely, the highest workload rating was observed in the *effort* dimension, with a mean of 16.4, reflecting the perceived work required to achieve the observed performance level. Among the primary demand subscales, *mental demand* received the highest rating (14.9), indicating that

cognitive processing constituted the primary component of user perceived effort. Nevertheless, overall workload ratings remained consistently low, with all subscale distributions in Fig. 28(c) falling within the low-to-very-low workload intervals.

The Task Average Completion Time (TACT) across all trials was 60.9 ± 12.0 s. For comparison, benchmark trials were conducted with an experienced driver, that worked on the development of MoviWE.Q, that was asked to drive MoviWE.Q on the same track in three different ways. First, the driver was asked to sit on the wheelchair and drive the system using the conventional 3-axis joystick mounted on the armrest. Five repetition were performed yielding to a TACT of 49.2 ± 5.1 s. Then, the experienced driver was asked to repeat the tests using the joystick while walking next to the wheelchair. Five repetition of this test were performed yielding to a TACT of 55.4 ± 4.8 s. Finally, the experienced driver repeated the test driving MoviWE.Q using the force-sensitive interface SensHB.Q. Five repetition of this test were performed yielding to a TACT of 46.7 ± 2.9 s.

Given the limited number of repetitions with experienced driver, the fact that only one experienced driver was involved, these data should be treated only as benchmarks. Nevertheless, interesting insights about the system seems to appear. As expected, the TACT seems to decrease with experience (unexperienced participants TACT 60.9 s, experienced driver TACT 46.7 s, reduction percentage of about 23.3%) suggesting that there is a learning curve associated to the interface, as there is with every drive-interface. Moreover, the experienced driver using SensHB can complete the task in about the same time as using a 3-axis joystick while seated on the wheelchair, suggesting comparable navigation efficiency. The TACT of the experienced driver using SensHB.Q seems to be lower than the TACT of the experienced driver using the 3-axis joystick while walking next to the wheelchair (reduction percentage of about 15.7%), suggesting that even an experienced driver can benefit from the force-sensitive interface. This result could be explained with the issued described in Section 1.3 and summarized in Fig. 6.

7. Conclusion

This paper presented the kinematic modeling, mechanical design, and experimental validation of MoviWE.Q, an innovative pseudo-omnidirectional electric-powered wheelchair (EPW) developed specifically for indoor mobility. To overcome the lateral mobility restrictions of traditional differential-drive wheelchairs as well as the drawbacks associated with discontinuous contact point and small roller diameter of special-wheeled systems (such as those based on mecanum and omni wheels), MoviWE.Q utilizes a mobile base equipped with two swerve-drive locomotion units for traction and two passive castor wheels for balance. The primary technical contributions of this work are highlighted as follows:

Kinematic modeling: A general kinematic formulation was established for platforms based on n-swerve locomotion units to relate platform velocity twist $\mathbf{V}_b$ to wheel actuation variables ($\delta_i, \dot{\theta}_i, \forall i = 1, \dots, n$). This model is based on pre-existing literature, and it has been included in the text as it is essential for the other analysis in Section 3. The kinematic model is based on rigid-body assumption under pure-rolling contact between the wheels and the ground. For inverse kinematics, an optimal solution selection algorithm based on unit-circle chord distances was proposed (novel contribution) to minimize steering joint rotation in presence of steering joints that can rotate without limitations. Applied to MoviWE.Q ($n = 2$, $r = 101$ mm, $a = 250$ mm), the non-skidding constraint simplifies to $s_{\delta_1}\dot{\theta}_1 = s_{\delta_2}\dot{\theta}_2$. Furthermore, novel contributions regarding the kinematic analysis involve a dimensionless analysis used to evaluate the achievable 3D velocity twist considering the effect of the maximum wheel angular velocity. Additionally, the steering velocity limit $\dot{\delta}_{\max}$ was shown to govern the minimum achievable curvature radius ($r_{curv,min} = \|\dot{\mathbf{p}}_b\|/|\dot{\delta}_{\max}|$) during pure-translational maneuvers.

Force-sensitive interface design: To provide caregivers with an intuitive driving experience without relying on costly multi-axis force/torque sensors (usually the price range is from €5000 to €12000), the SensHB.Q sensorized handlebar was developed. Based on a planar 3-DOF six-bar linkage mechanism, the design uses three low-cost uniaxial load cells (∼ 150€ each) to measure the applied wrench components (M_z, F_x, F_y). The price comparison is based on the force sensors as they represent the most expensive part of the interface. In fact, all the other parts of SensHB.Q are 3-D printed components and low-cost electronics. The prototype features a monolithic 3D-printed structure with compliant flexure hinges that eliminate joint static friction and reduce part count down to three main components, the mechanism body and the two ergonomic handles. Integrated capacitive touch sensors serve as dead-man switches for safety. Applied wrenches are converted into smooth velocity twist references through a Coulomb dry-friction dynamic estimator model with manually-tuned physical parameters.

Experimental validation: ISO 7176-5 testing confirmed a compact profile (41 kg total mass, 630 mm width) and a pivot width of 1050 mm (well below the 1400 mm ISO limit). Bench validation of SensHB.Q against a commercial six-axis sensor demonstrated high accuracy with low RMS errors (1.95 N for F_x, 1.92 N for F_z, and 0.16 Nm for M_y). Finally, caregiver driving trials involving 18 volunteers achieved a 100% task completion rate, a System Usability Scale (SUS) mean score of 83.1 (suggesting good-to-excellent usability), and a NASA-TLX score of 10.9, suggesting low perceived workload. It should be underlined that the participants population does not include professional caregivers and that no real-case applications have been studied. Thus, these promising results should be intended as an initial assessment under the laboratory conditions tested.

Future work will focus on expanding the platform's capabilities by implementing and testing an autonomous navigation drive mode that works in cooperation with the user driving intention preventing collisions with obstacles and other people even in manual drive mode. Moreover, the experimental campaign will be expanded conducting extended field trials in real-world care facilities with end-users and professional caregivers.

CRediT authorship contribution statement

Luigi Tagliavini: Writing – original draft, Validation, Formal analysis, Data curation, Conceptualization; **Andrea Botta:** Writing – review & editing, Validation, Methodology; **Giovanni Colucci:** Writing – review & editing, Methodology, Formal analysis; **Lorenzo**

Baglieri: Writing – review & editing, Validation, Software; **Simone Duretto:** Writing – review & editing, Validation, Methodology; **Lorenzo Toccaceli:** Writing – review & editing, Validation; **Francesco Amodio:** Writing – review & editing, Validation; **Giuseppe Quaglia:** Writing – review & editing, Project administration, Conceptualization.

Ethical statement

The experimental protocol involving human participants was reviewed and approved by the Ethics Committee of the University (Protocol No. 66459/2026, Approval No. 59521/2026). Informed consent was obtained from all individual participants included in the study.

Declaration of generative AI in the manuscript preparation process

During the preparation of this work the authors used the tool ImageGen integrated in ChatGPT (GPT-6) to create the base images for Fig. 6. Only the illustrations of the man pushing the wheelchair and the joystick in the straight and tilted configurations are the result of generative AI. These base illustrations were subsequently edited by the authors, layered, and composed into a vector diagram using an open-source software for vector graphics.

Declaration of competing interest

The authors declare that they have no known competing financial interests or personal relationships that could have appeared to influence the work reported in this paper.

Data availability

Data will be made available on request.

References

[1] M. Sander, B. Oxlund, A. Jespersen, A. Krasnik, E.L. Mortensen, R.G.J. Westendorp, L.J. Rasmussen, et al., The challenges of human population ageing, Age Ageing 44 (2) (2015) 185–187.
[2] World Health Organization (WHO), Ageing: Global population, 2025, (Questions and answers). Updated 21 February 2025. Accessed on 8 May 2026.
[3] G.C. Brown, Living too long, EMBO Rep. 16 (2) (2015) 137–141. https://doi.org/10.15252/embr.201439518
[4] World Health Organization (WHO), Ageing and health, 2025, (Fact sheet). Updated 1 October 2025. Accessed on 8 May 2026.
[5] Istituto Nazionale di Statistica (ISTAT), Indicatori demografici | Anno 2025: Popolazione stabile grazie alle migrazioni. Continua il calo della fecondità e aumenta la speranza di vita, Technical Report, ISTAT, Rome, 2026. Provisional data. Published March 2026. Accessed on 8 May 2026.
[6] World Health Organization (WHO), Assistive technology, 2024, (Fact sheet). Accessed on 8 May 2026.
[7] World Health Organization (WHO), Global report on health equity for persons with disabilities, Technical Report, World Health Organization, Geneva, 2022. Accessed on 8 May 2026. License: CC BY-NC-SA 3.0 IGO.
[8] Istituto Nazionale di Statistica (ISTAT), Le condizioni di salute della popolazione anziana in Italia - Anno 2019, Technical Report, ISTAT, 2021. Accessed on 8 May 2026.
[9] World Health Organization (WHO), United Nations Children's Fund (UNICEF), Global report on assistive technology, Technical Report, World Health Organization, Geneva, 2022. Licence: CC BY-NC-SA 3.0 IGO.
[10] United Nations, Disability and Development Report 2024: Accelerating the realization of the Sustainable Development Goals by, for and with persons with disabilities, Technical Report, United Nations Department of Economic and Social Affairs (UN DESA), New York, 2024. Advance Unedited Version. Sales No. E.23.IV.3. Accessed on 8 May 2026.
[11] Istituto Nazionale di Statistica (ISTAT), L'inclusione scolastica degli alunni con disabilità | Anno scolastico 2023–2024, Technical Report, ISTAT, Rome, 2025. Accessed on 8 May 2026.
[12] J.D. Mozingo, M. Akbari-Shandiz, N.S. Murthy, M.G. Van Straaten, B.A. Schueler, D.R. Holmes, III, C.H. McCollough, K.D. Zhao, Shoulder mechanical impingement risk associated with manual wheelchair tasks in individuals with spinal cord injury, Clin. Biomech. 71 (2020) 221–229.
[13] P. Cavallone, E. Bonisoli, G. Quaglia, Handwheelchair. Q: new prototype of manual wheelchair for everyday life, in: Advances in Italian Mechanism Science: Proceedings of the 3rd International Conference of IFToMM Italy 3, Springer, 2021, pp. 111–119.
[14] P. Cavallone, A. Botta, E. Bonisoli, G. Quaglia, Preliminary experimental test of a cable-driven wheelchair in different configurations, in: Proceedings of I4SDG Workshop 2021: IFToMM for Sustainable Development Goals 1, Springer, 2022, pp. 166–173.
[15] S.A. Sundaram, H. Wang, D. Ding, R.A. Cooper, Step-climbing power wheelchairs: a literature review, Top. Spinal Cord Inj. Rehabil. 23 (2) (2017) 98–109.
[16] C. Chen, H. Pham, Design and fabrication of a statically stable stair-climbing robotic wheelchair, Ind. Robot 36 (6) (2009) 562–569. https://doi.org/10.1108/01439910910994632
[17] K. Sugihara, S. Fujimoto, K. Yoshida, Development of electric wheelchair with input of force feedback joystick, in: MATEC Web of Conferences, 51, EDP Sciences, 2016, p. 02008.
[18] J. Yuan, Stability analyses of wheelchair robot based on "human-in-the-loop" control theory, in: 2008 IEEE International Conference on Robotics and Biomimetics, IEEE, 2009, pp. 419–424.
[19] G. Quaglia, W. Franco, R. Oderio, Wheelchair. q, a motorized wheelchair with stair climbing ability, Mech. Mach. Theory 46 (11) (2011) 1601–1609.
[20] T. Yamamoto, F. Takemori, R. Itakura, Development of stair locomotive wheelchair with adjustable wheelbase, in: 2012 Proceedings of SICE Annual Conference (SICE), IEEE, 2012, pp. 629–633.
[21] Y.-b. Bang, C.-h. Lee, J.-h. Yoo, K.-m. Lee, I.-s. Kim, Two-legged stair-climbing wheelchair and its stair dimension measurement using distance sensors, in: 2011 11th International Conference on Control, Automation and Systems, IEEE, 2011, pp. 1788–1791.
[22] R. Morales, V. Feliu, A. Gonzalez, P. Pintado, Kinematic model of a new staircase climbing wheelchair and its experimental validation, Int. J. Robot. Res. 25 (9) (2006) 825–841.
[23] W. Tao, J. Xu, T. Liu, Electric-powered wheelchair with stair-climbing ability, Int. J. Adv. Robot. Syst. 14 (4) (2017) 1729881417721436.
[24] S. Yu, T. Wang, X. Li, C. Yao, Z. Wang, D. Zhi, Configuration and tip-over stability analysis for stair-climbing of a new-style wheelchair robot, in: 2010 IEEE International Conference on Mechatronics and Automation, IEEE, 2010, pp. 1387–1392.
[25] Quickie-Wheelchairs, Quickie Q100R REAR-WHEELED POWERCHAIR, 2022.

[26] Quickie-Wheelchairs, Quickie Q500M Power Wheelchair Bundle, 2022.
[27] Permobil, Permobil F3 Corpus, 2022.
[28] Senior, Foldawheel 4X4 All Terrain Indoor Outdoor 4 Wheel Drive Stair Climbing Gyroscope Power Electric Wheelchair, 2022.
[29] A.S. Kundu, O. Mazumder, P.K. Lenka, S. Bhaumik, Omnidirectional assistive wheelchair: design and control with isometric myoelectric based intention classification, Procedia Comput. Sci. 105 (2017) 68–74.
[30] K. Matsuo, L. Barolli, Design and implementation of an omnidirectional wheelchair: control system and its applications, in: 2014 Ninth International Conference on Broadband and Wireless Computing, Communication and Applications, IEEE, 2014, pp. 532–535.
[31] Y. Li, S. Dai, Y. Zheng, F. Tian, X. Yan, Modeling and kinematics simulation of a Mecanum wheel platform in RecurDyn, J. Robot. 2018 (2018).
[32] B. Adamov, Influence of mecanum wheels construction on accuracy of the omnidirectional platform navigation (on exanple of KUKA youBot robot), in: 2018 25th Saint Petersburg International Conference on Integrated Navigation Systems (ICINS), 2018, pp. 1–4. https://doi.org/10.23919/ICINS.2018.8405889
[33] M. Wada, H.H. Asada, Design and control of a variable footprint mechanism for holonomic omnidirectional vehicles and its application to wheelchairs, IEEE Trans. Robot. Autom. 15 (6) (1999) 978–989.
[34] Q.-U. of-Science-and Technology, Omnidirectional wheelchair with automatically adjustable gravity center, China Patent CN113440345A, Sept. 2021.
[35] T. Konrad, Der Omnichair - Elektrorollstuhl der neuen Generation, 2016.
[36] P.L. D.C. Ribeiro, I.M.C. Silva, N.S. S.M. Moutinho, P.A. S.B. Pereira, Oomnidirectional wheelchair electrical control system, Spanish Patent ES2331554B1, Gen. 2010.
[37] C. Torkia, D. Reid, N. Korner-Bitensky, D. Kairy, P.W. Rushton, L. Demers, P.S. Archambault, Power wheelchair driving challenges in the community: a users' perspective, Disabil. Rehabil. Assist. Technol. 10 (3) (2015) 211–215.
[38] Slowmoose, Unviersal conversion and replacemetns parts power wheelchair joystick.
[39] Permobil, Softball, Handles.
[40] Permobil, T-Handles.
[41] Permobil, Stick Joystick Handle.
[42] Permobil, Bodypoint Dome-Shaped Handle.
[43] Permobil, Bodypoint U-Shaped Handle.
[44] Permobil, Large Ball Handle.
[45] Permobil, Chin Cup, Handles.
[46] A. Ghorbel, N.B. Amor, M. Jallouli, A survey on different human-machine interactions used for controlling an electric wheelchair, Procedia Comput. Sci. 159 (2019) 398–407.
[47] V.H. Andaluz, J.S. Ortiz, F.A. Chicaiza, J. Varela, E.G. Espinosa, P. Canseco, Adaptive control of the human-wheelchair system through brain signals, in: Intelligent Robotics and Applications: 9th International Conference, ICIRA 2016, Tokyo, Japan, August 22–24, 2016, Proceedings, Part II 9, Springer, 2016, pp. 223–234.
[48] J.-S. Lin, S. Cheng-Hung, An ssvep-based bci system and its applications, Int. J. Adv. Comput. Sci. Appl. 5 (10) (2014) 54–60.
[49] L. Cao, J. Li, H. Ji, C. Jiang, A hybrid brain computer interface system based on the neurophysiological protocol and brain-actuated switch for wheelchair control, J. Neurosci. Methods 229 (2014) 33–43.
[50] L. Tonin, S. Perdikis, T.D. Kuzu, J. Pardo, B. Orset, K. Lee, M. Aach, T.A. Schildhauer, R. Martínez-Olivera, R. Millán José del, Learning to control a BMI-driven wheelchair for people with severe tetraplegia, Iscience 25 (12) (2022) 105418.
[51] S.H. Healthcare, Sip-N-Puff, Stationary.
[52] I. Mougharbel, R. El-Hajj, H. Ghamlouch, E. Monacelli, Comparative study on different adaptation approaches concerning a sip and puff controller for a powered wheelchair, in: 2013 Science and Information Conference, IEEE, 2013, pp. 597–603.
[53] N.I. Katevas, N.M. Sgouros, S.G. Tzafestas, G. Papakonstantinou, P. Beattie, J.M. Bishop, P. Tsanakas, D. Koutsouris, The autonomous mobile robot SENARIO: a sensor aided intelligent navigation system for powered wheelchairs, IEEE Robot. Autom. Mag. 4 (4) (1997) 60–70.
[54] S.P. Levine, D.A. Bell, L.A. Jaros, R.C. Simpson, Y. Koren, J. Borenstein, The NavChair assistive wheelchair navigation system, IEEE Trans. Rehabil. Eng. 7 (4) (1999) 443–451.
[55] M.R. Walter, S. Hemachandra, B. Homberg, S. Tellex, S. Teller, A framework for learning semantic maps from grounded natural language descriptions, Int. J. Robot. Res. 33 (9) (2014) 1167–1190.
[56] J. Kim, H. Park, J. Bruce, E. Sutton, D. Rowles, D. Pucci, J. Holbrook, J. Minocha, B. Nardone, D. West, et al., The tongue enables computer and wheelchair control for people with spinal cord injury, Sci. Transl. Med. 5 (213) (2013) 213ra166–213ra166.
[57] F.B. Taher, N.B. Amor, M. Jallouli, A.B. Hammouda, O. Dghim, A collaborative and voice configured electric powered wheelchair control system based on eeg and head movement, in: 3rd International Conference on Automation, Control Engineering and Computer Science, 2016.
[58] R. Berjón, M. Mateos, A. Barriuso, I. Muriel, G. Villarrubia, Head tracking system for wheelchair movement control, in: Highlights in Practical Applications of Agents and Multiagent Systems: 9th International Conference on Practical Applications of Agents and Multiagent Systems, Springer, 2011, pp. 307–315.
[59] S. Plesnick, D. Repice, P. Loughnane, Eye-controlled wheelchair, in: 2014 IEEE Canada International Humanitarian Technology Conference-(IHTC), IEEE, 2014, pp. 1–4.
[60] B. Thakur, K. Kulshrestha, Eye controlled electric wheelchair, in: 2014 IEEE International Conference on Computational Intelligence and Computing Research, IEEE, 2014, pp. 1–6.
[61] Munevo, Munevo Drive.
[62] T. Suzuki, H. Uchiyama, C. Holloway, N. Tyler, Assisting control for attendant propelled wheelchair based on force velocity relationship, in: 2012 Annual International Conference of the IEEE Engineering in Medicine and Biology Society, IEEE, 2012, pp. 3073–3076.
[63] A. Kakimoto, H. Matsuda, Y. Sekiguchi, Development of power-assisted attendant-propelled wheelchair, in: Proceedings of the 19th Annual International Conference of the IEEE Engineering in Medicine and Biology Society.'Magnificent Milestones and Emerging Opportunities in Medical Engineering'(Cat. No. 97CH36136), 4, IEEE, 1997, pp. 1875–1876.
[64] H. Kitagawa, K. Terashima, T. Miyoshi, J. Urbano, S. Nishisaka, Power assist system for omni-directional transport wheelchair using fuzzy reasoning, in: Proceedings of the 2004 IEEE International Conference on Control Applications, 2004., 1, IEEE, 2004, pp. 123–130.
[65] C. Zhu, M. Oda, M. Yoshioka, T. Nishikawa, S. Shimazu, X. Luo, Admittance control based walking support and power assistance of an omnidirectional wheelchair typed robot, in: 2010 IEEE International Conference on Robotics and Biomimetics, IEEE, 2010, pp. 381–386.
[66] S. Katsura, K. Ohnishi, A wheelchair type mobile robot taking environmental disturbance into account, in: 7th International Workshop on Advanced Motion Control. Proceedings (Cat. No. 02TH8623), IEEE, 2002, pp. 500–505.
[67] A. Trujillo-León, W. Bachta, J. Castellanos-Ramos, F. Vidal-Verdú, Assistive handlebar based on tactile sensors: control inputs and human factors, Sensors 18 (8) (2018) 2471.
[68] I.-S. Weon, S.-G. Lee, Recognition of user's gait intenstion for a walking assist system using pressure-sensing handlebars, in: 2017 First IEEE International Conference on Robotic Computing (IRC), IEEE, 2017, pp. 326–329.
[69] F. Shi, Q. Cao, C. Leng, H. Tan, Based on force sensing-controlled human-machine interaction system for walking assistant robot, in: 2010 8th World Congress on Intelligent Control and Automation, IEEE, 2010, pp. 6528–6533.
[70] A. Cirillo, P. Cirillo, G. De Maria, C. Natale, S. Pirozzi, A distributed tactile sensor for intuitive human-robot interfacing, J. Sens. 2017 (2017) 1893–1898.
[71] L. Zhang, Q.X. Cao, C.T. Leng, A.L. Tang, F. Shi, The development of walking assistant robot for the elderly, in: Key Engineering Materials, 467, Trans Tech Publ, 2011, pp. 1893–1898.
[72] K. Yamada, K. Ohara, A. Ichikawa, T. Fukuda, User intention estimation by grip sensor for cane-type walking support robot, in: 2016 International Symposium on Micro-NanoMechatronics and Human Science (MHS), IEEE, 2016, pp. 1–3.
[73] L. Tagliavini, G. Quaglia, On the design of MoviWE. Q: an omnidirectional electric-powered wheelchair for indoor mobility, in: IFToMM World Congress on Mechanism and Machine Science, Springer, 2023, pp. 311–321.

[74] L. Tagliavini, G. Quaglia, SensHB.Q: a cost-effective force-sensitive handlebar to control omnidirectional robots and wheelchairs, J. Field Robot. (2025). https://doi.org/10.1002/rob.70104
[75] L. Tagliavini, G. Colucci, A. Botta, P. Cavallone, L. Baglieri, G. Quaglia, Wheeled mobile robots: state of the art overview and kinematic comparison among three omnidirectional locomotion strategies, J. Intell. Robot. Syst. 106 (3) (2022) 57.
[76] G. Campion, G. Bastin, B. D'Andrea-Novel, Structural properties and classification of kinematic and dynamic models of wheeled mobile robots, in: [1993] Proceedings IEEE International Conference on Robotics and Automation, (vol.1), 1993, pp. 462–469. https://doi.org/10.1109/ROBOT.1993.292023
[77] K.M. Lynch, F.C. Park, Modern Robotics: Mechanics, Planning, and Control, Cambridge University Press, Cambridge, UK, Cambridge, UK, 2017.
[78] J. Brooke, SUS-A quick and dirty usability scale, Usability Eval. Ind. 189 (194) (1996) 4–7.
[79] M. Callejas-Cuervo, A.X. González-Cely, T. Bastos-Filho, Design and implementation of a position, speed and orientation fuzzy controller using a motion capture system to operate a wheelchair prototype, Sensors 21 (13) (2021) 4344.
[80] A.M. Panchea, N. Todam Nguepnang, D. Kairy, F. Ferland, Usability evaluation of the smartwheeler through qualitative and quantitative studies, Sensors 22 (15) (2022) 5627.
[81] X. Zhang, J. Li, L. Jin, J. Zhao, Q. Huang, Z. Song, X. Liu, D.-B. Luh, Design and evaluation of the extended FBS model based gaze-control power wheelchair for individuals facing manual control challenges, Sensors 23 (12) (2023) 5571.
[82] S.G. Hart, L.E. Staveland, Development of NASA-TLX (task load index): results of empirical and theoretical research, in: Advances in Psychology, 52, Elsevier, 1988, pp. 139–183.
[83] S.G. Hart, NASA-Task load index (NASA-TLX); 20 years later, in: Proceedings of the Human Factors and Ergonomics Society Annual Meeting, 50, Sage publications Sage CA: Los Angeles, CA, 2006, pp. 904–908.



Luigi Tagliavini is an Assistant Professor (RTDA) in the Department of Mechanical and Aerospace Engineering (DIMEAS) at Politecnico di Torino, Italy. He received his B.Sc. in Mechanical Engineering in 2018 at Università degli Studi di Ferrara, his M.Sc. in Mechanical Engineering in 2020 at Politecnico di Torino, and his Ph.D. in Mechanical Engineering in 2024 at Politecnico di Torino. His research interest lies in the design and the development of innovative mobile service robots and assistive technologies.



Andrea Botta is assistant Professor (RTDA) at Politecnico di Torino, Italy. Enrolled as a student at Politecnico di Torino, he received his BSc in Mechanical engineering in 2014, MSc in Mechatronic Engineering in 2017, and PhD in Mechanical Engineering in 2022 at Politecnico di Torino. In 2023, he held a postdoc position at Tokyo Institute of Technology funded by the Japanese Society for the Promotion of Science (JSPS) in 2023. His research activities are oriented towards sustainable development and the achievement of the Sustainable Development Goals. In particular, the research interest lies in the design and the development of innovative mobile service robots, with a focus on precision agriculture, and assistive and rehabilitative devices for the elderly, people with disabilities or people recovering from injuries.



Giovanni Colucci is an Assistant Professor (RTDA) in the Department of Mechanical and Aerospace Engineering (DIMEAS) at Politecnico di Torino. He received his BSc in Industrial Engineering in 2018 at Università del Salento in Lecce, his MSc in Mechanical Engineering in 2021 and his Ph.D. in Mechanical Engineering in 2025 at Politecnico di Torino. His research activities regard Service Robotics and Soft Robotics.



Lorenzo Baglieri received the B.Sc. and M.Sc. degrees in Mechanical Engineering from Politecnico di Torino, Italy, in 2019 and 2021, respectively, and the Ph.D. degree in Mechanical Engineering with honours in 2026, under a joint supervision agreement between Politecnico di Torino and the Institute of Science Tokyo, Japan. His doctoral research focused on hands-free human-machine interfaces for omnidirectional electric-powered wheelchairs, combining vision, inertial and proximity sensing with learning-based estimation of user intention. He has also contributed to the design and development of mobile service robots for healthcare and agricultural applications, including the robotic arm, autonomous navigation module and sensing system of the PAQUITOP hospital mobile manipulator. He has co-authored more than 35 peer-reviewed publications, seven of them as first author. His research interests include mobile service robotics, assistive technologies, human-robot interaction, computer vision, autonomous navigation and learning by demonstration for mobile manipulation.



Simone Duretto is a PhD candidate at Politecnico di Torino, Italy, in the Department of Mechanical and Aerospace Engineering (DIMEAS). He received his Bachelor's and Master's degrees in Mechanical Engineering from Politecnico di Torino, in 2021 and 2023, respectively. His research interests include soft actuators, tactile sensors for robotic manipulation, and haptic technologies.



Lorenzo Toccaceli is a Ph.D. candidate at Politecnico di Torino, Italy, in the Department of Mechanical and Aerospace Engineering (DIMEAS). He received his B.Sc. in Mechanical Engineering in 2019 at Università degli Studi di Salerno in Fisciano, his M.Sc. in Mechanical Engineering in 2023 at Politecnico di Torino. His research interests are in the field of Service Robotics, with a particular focus on the design and development of mobile robots for inspection and search-and-rescue operations.



Francesco Amodio received his M.Sc. degree in Automotive Engineering in 2024 from Politecnico di Torino, Turin, Italy, where he is currently a Ph.D. candidate in the Department of Mechanical and Aerospace Engineering (DIMEAS). His research interests focus on mobile robotics, terramechanics, tribology and cable-driven parallel manipulators.



Giuseppe Quaglia is a full professor of Applied Mechanics at Politecnico di Torino, Italy. His scientific activity is mainly related to: energy saving, renewable energy and sustainability, vehicle dynamic and systems, robotics and mechatronics, automation, actuators and mechanisms, device for disabled people and biomedical applications, appropriate technologies and systems for sustainable human development. Moreover, he had the scientific responsibility of competitive National and International research projects, awarded through a peer-review process. Prof. Quaglia was leading research projects between the Politecnico di Torino and several industries. The results of applied research and technological transfer are evidenced by the presence of 16 patents, indicating the originality and innovative nature of the research activity.